



JÖNKÖPING UNIVERSITY
School of Engineering

Licentiate Thesis

Iron Refining in Recycled Al-Si Alloys by Intermetallic Precipitation

Abdullah Harazeen

Jönköping University
School of Engineering
Dissertation Series No. 101 • 2026



JÖNKÖPING UNIVERSITY
School of Engineering

Licentiate Thesis

Iron Refining in Recycled Al-Si Alloys by Intermetallic Precipitation

Abdullah Harazeen

Licentiate thesis in Materials and Manufacturing

Iron Refining in Recycled Al-Si Alloys by Intermetallic Precipitation
Dissertation Series No. 101

©2026 Abdullah Harazeen

Published by
School of Engineering, Jönköping University
P.O. Box 1026
SE-551 11 Jönköping
Tel. +46 36 10 10 00
www.ju.se

Printed by Stema Specialtryck AB 2026

ISBN 978-91-89785-35-9 (Printed version)
ISBN 978-91-89785-36-6 (Online version)



Acknowledgements

I wish to express my heartfelt appreciation to:

My main supervisor, Professor Anders E. W. Jarfors, for his guidance, input and fruitful discussions throughout this work.

My co-supervisor, Dr Lucia Lattanzi, for her insightful feedback, scientific rigour and encouragement throughout this work.

My co-supervisor, Dr Taishi Matsushita, for constructive discussions and valuable feedback that greatly enhanced the depth and rigour of this work.

Esbjörn Ollas, Jacob Steggo, and Jörgen Bloom for your support in developing the experimental setup and for your guidance in using laboratory tools and equipment.

Jönköping University, Vinnova and Metalliska material Programme for establishing the necessary financial conditions to run the KlirAl project.

All the KlirAl project partners and members for their support, provision of the required raw materials, and valuable discussions and continuous collaboration throughout this work.

All my colleagues and friends in the Materials and Manufacturing department for creating a supportive research environment.

My family, for always being there for me and providing me with a consistent motivational boost.

Abdullah Harazeen

Jönköping 2026

Abstract

Aluminium production is expected to increasingly depend on recycled aluminium, driven by lower energy costs and the need to reduce carbon footprints as environmental regulations and policies become stricter. One of the main limitations of recycling aluminium, mainly aluminium-silicon (Al-Si) alloys, is the high iron (Fe) concentration. Fe forms the β -Al₅SiFe phase, which has a plate-like morphology with sharp edges that severely degrades both castability and the mechanical properties of the cast Al.

A promising approach for Fe refining is through the addition of Fe-bearing intermetallic particle formers, such as manganese (Mn), chromium (Cr) and strontium (Sr). The main aim of this research is to develop a quantitative understanding of Fe removal in low-Fe Al-Si alloys by investigating the formation and sedimentation behaviour of Fe-bearing intermetallic particles under different Mn, Cr, and Sr combinations. To do so, a series of small-scale experiments was conducted using 8 kg of molten Al-11Si-0.5Fe alloy.

The results demonstrated that, for a low-Fe Al-Si alloy, a relationship between Fe removal efficiency and the Fe-bearing intermetallic particles was established by calculating the Fe removal potential. When comparing the Fe removal potential with the clean aluminium yield, a clear trade-off was noticed. The higher Fe removal efficiency results in lower clean aluminium yield (Mn-Cr addition) and vice versa (Mn-Sr/Mn-only additions).

To further understand the effect of cooling rate on Fe-bearing intermetallic particles, a physics-based growth-sedimentation model was developed and calibrated using experimental results to quantitatively describe the coupled evolution of particle size and settling behaviour at different cooling rates. The model showed that the 1.5Mn0.6Cr addition results in a lower yield due to increased resistive forces arising from viscosity, tortuosity, particle-particle interactions, and drag. While in 1.5Mn and 1.2Mn0.3Sr, a higher yield was obtained due to their compact morphology and more effective sedimentation.

Keywords: Al-Si alloy, Fe removal, Fe-bearing intermetallic particles, sedimentation, cleaning and refining.

Sammanfattning

Aluminiumproduktion förväntas i allt högre grad bestå av återvunnet aluminium, drivet av lägre energikostnader och behovet av att minska koldioxidavtrycket, i takt med att miljöregler och policyer blir allt mer krävande. En av de största begränsningarna med återvinning av aluminium, främst aluminium-kisel (Al-Si)-legeringar, är närvaron av järn (Fe) i återvunnet aluminium. Fe bildar β -Al₅SiFe-fasen, som har en plattliknande morfologi med skarpa hörn och kanter som kraftigt försämrar både gjutbarheten och de mekaniska egenskaperna hos den aluminiumlegeringar.

En lovande metod för Fe-rening är genom tillsats av legeringselement som bildar intermetalliska partiklar som innehåller Fe, såsom mangan (Mn), krom (Cr) och strontium (Sr). Huvudsyftet med detta arbete är att utveckla kvantitativ förståelse för Fe-rening i Al-Si-legeringar med låg Fe-halt genom att undersöka bildnings- och sedimentationsförloppet hos Fe-innehållande intermetalliska partiklar under olika Mn-, Cr- och Sr-kombinationer och halter. För att göra detta genomfördes en serie småskaliga experiment med 8 kg smält Al-11Si-0.5Fe-legering.

För en Al-Si-legering med låg Fe-halt fastställdes ett samband mellan Fe-reningseffektiviteten och de Fe-bärande intermetalliska partiklarna genom att beräkna Fe-reningspotentialen. Vid jämförelse av Fe-reningspotentialen med utbytet av renat aluminium identifierades ett vägval. Den högre Fe-reningseffektiviteten resulterar i lägre utbyte av rent aluminium (Mn-Cr-tillsats) och vice versa (Mn-Sr/enda Mn-tillsatser) kopplat till partiklarnas karaktär.

För att ytterligare förstå effekten av svalningshastigheten på de Fe-innehållande intermetalliska partiklarna utvecklades och kalibrerades en fysikaliskt baserad tillväxt-sedimentationsmodell med stöd av experimentella resultat för att kvantitativt beskriva den kopplade partikeltillväxten och sedimenteringsbeteendet vid olika kylningshastigheter. Modellen visade att tillsatsen av 1.5Mn0.6Cr resulterar i ett lägre utbyte kopplat till viskositet, flödesmotstånd beroende på partikelformen. Vidare påverkar partikel-partikel-interaktioner och packningsgraden i sedimentet. I kontrast till 1.5Mn

0.6Cr så ger en 1.5Mn och 1.2Mn0.3Sr ett högre utbyte på grund av deras mer kompakta partikelmorfologi och därmed även mer effektiva sedimentering och packning i sedimentet.

Nyckelord: Al-Si-legering, Fe-rening, Fe-innehållande intermetalliska partiklar, sedimentation, rening och avlägsnande.

Supplements

The following papers are enclosed as appendices.

Supplement I

A. Harazeen, L. Lattanzi, T. Matsushita, A.E.W. Jarfors, Enhanced iron impurity removal in low iron Al-Si alloys by Mn addition, *High Temperatures-High Pressures* 54 (2025) 187–201.

<https://doi.org/10.32908/hthp.v54.1905>.

All authors contributed to the conception, experimental design, and setup. A. Harazeen performed material preparation, data collection, analysis and wrote the first draft of the manuscript. L. Lattanzi, T. Matsushita and A.E.W. Jarfors provided guidance on the analysis of data and review of the manuscript.

Supplement II

A. Harazeen, L. Lattanzi, T. Matsushita, A.E.W. Jarfors, Iron Removal from Recycled Al-Si alloys by Cr, Sr and Mn Additions, under review in *International Journal of Metalcasting*.

All authors contributed to the conception, experimental design, and setup. A. Harazeen performed material preparation, data collection, analysis and wrote the first draft of the manuscript. L. Lattanzi, T. Matsushita and A.E.W. Jarfors provided guidance on the analysis of data and review of the manuscript.

Supplement III

A. Harazeen, T. Matsushita, A.E.W. Jarfors, Settling and Growth of Fe-bearing Intermetallic Particles in Recycled Al-Si Alloys, submission-ready manuscript.

All authors contributed to the conception, experimental design, and setup. A. Harazeen performed material preparation, data collection, analysis and wrote the first draft of the manuscript. A. Harazeen and T. Matsushita created the growth-sedimentation model. A.E.W. Jarfors and T. Matsushita provided guidance on the analysis of data and review of the manuscript.

Table of Contents

1	Introduction	1
1.1	Background	1
1.2	Aluminium	2
1.2.1	Aluminium production	2
1.2.2	Classification of aluminium alloys.....	3
1.2.3	Aluminium-silicon (Al-Si) alloys.....	3
1.3	Sustainable aluminium production	5
1.3.1	Aluminium recycling.....	5
1.3.2	Aluminium recycling limitation	6
1.3.3	Iron as a limiting impurity in Al-Si alloys.....	7
1.4	Current strategies for Fe mitigation and their limitations.....	8
1.4.1	Upstream control: scrap sorting and dilution	8
1.4.2	Melt treatment techniques	9
1.4.3	Alternative purification techniques	10
1.4.4	Alloying strategies	11
1.5	Knowledge gap.....	13
1.5.1	Research focus	14
2	Research Approach	15
2.1	Purpose and aim of the research.....	15
2.1.1	Reflection on the chosen method	15
2.2	Research design.....	16
2.2.1	Research perspective	16
2.2.2	Research methodology	16
2.2.3	Research questions	17
2.3	Material and experimental procedures	19
2.3.1	Alloys	20
2.3.2	Sample preparation.....	21
2.3.3	Sample and alloy testing	23
2.3.4	Material characterisation and evaluation.....	23
2.3.5	Modelling methodology	24

3	Results and Discussion	26
3.1	Equilibrium and experimental chemical analysis of alloy addition on Fe removal.....	26
3.1.1	Equilibrium calculation	26
3.1.2	Chemical analysis.....	27
3.1.3	Chemical analysis vs equilibrium calculation	30
3.2	Microstructural evaluation of Fe-bearing intermetallic under different alloy additions	33
3.2.1	Comparison between Mn-only and Mn-Cr additions	35
3.2.2	Comparison between Mn-Cr and Mn-Sr additions.....	38
3.3	Growth and sedimentation behaviour of the Fe-bearing intermetallic particles	42
4	Conclusion	49
5	Future Work	51
	References	53

1 Introduction

Chapter introduction

This chapter provides the background, motivation and research focus of this thesis, with emphasis on iron (Fe) impurity issues and current mitigation strategies in recycled aluminium-silicon (Al-Si) alloys.

1.1 Background

Currently, aluminium plays a crucial role in the automotive and aerospace industries due to its high strength-to-weight ratio, high corrosion resistance, and excellent electrical and thermal conductivity [1,2]. In addition, the mechanical properties could be tailored through alloying. As a result, the demand for aluminium has increased, leading to a significant expansion of primary aluminium production. At the same time, the aluminium industry is facing increasing pressure to reduce the environmental impact of aluminium production, as primary aluminium production is energy-intensive and contributes significantly to global greenhouse gas emissions [3,4].

One of the most effective ways to reduce the carbon footprint of aluminium production and support the circular economy is through aluminium recycling, as secondary aluminium production emits about 0.6 kg of CO₂ per kg of aluminium, compared to about 12 kg of CO₂ per kg of primary aluminium [5,6].

Consequently, aluminium production is expected to increasingly depend on recycled aluminium, driven by lower energy costs and the need to reduce carbon footprints as environmental regulations and policies become stricter. These policies and regulations aim to reduce greenhouse gas emissions in line with international agreements [7]. This places intense pressure on energy-intensive industries, such as aluminium production, to reduce their carbon footprint.

However, continuous recycling leads to a progressive accumulation of impurities from mixed or downgraded scrap. These impurities promote the formation of various intermetallic phases that reduce melt fluidity, increase porosity, and impair machinability, thereby negatively affecting the material's mechanical properties [8–10].

In Al-Si alloys, which are most commonly used in aluminium casting [11,12], high concentrations of iron (Fe) are the most problematic, as Fe forms the β -Al₅SiFe phase. The β -Al₅SiFe phase has a plate-like morphology with sharp edges, which has detrimental effects on both castability and the mechanical properties of the cast aluminium [13]. One promising Fe reduction method is the addition of Fe-bearing intermetallic particle formers, such as manganese (Mn) and chromium (Cr) [14,15]. The addition of these alloys promotes the transformation of the harmful β -Al₅SiFe phase to a less harmful phase that could later be removed through either sedimentation or filtration [13].

Despite substantial literature on the use of Fe-bearing intermetallic particle formers to reduce the Fe content in Al-Si alloys [13–15], critical uncertainties remain regarding their effectiveness at low Fe concentrations, especially regarding the formation, morphology, and sedimentation behaviour of the Fe-bearing intermetallic particles.

1.2 Aluminium

1.2.1 Aluminium production

Aluminium can be produced either through primary or secondary production. Primary aluminium is produced through the chemical refining of bauxite ore to alumina, followed by the electrolysis reduction. Bauxite ore is a naturally occurring ore, primarily composed of hydrated aluminium oxides and hydroxides, together with impurities (like iron oxides and silica). Bauxite ore is refined by the Bayer process to produce alumina (Al₂O₃). This process involves the alkaline extraction of Al₂O₃ using sodium hydroxide at elevated temperature and pressure, followed by the separation of insoluble residuals (red mud) [16,17].

The alumina generated by the Bayer process is then used to produce aluminium via the Hall-Héroult process. In the Hall-Héroult process, alumina is dissolved in molten cryolite-based electrolyte and then reduced by electrolysis. In the electrolysis process, an electric current is passed through the electrodes to separate alumina into aluminium. Molten aluminium is produced at the cathode, while oxygen released from the alumina will react with the carbon anode and produce carbon dioxide (CO₂), formed from the reaction of oxygen with the carbon anode [18]. On the other hand, secondary aluminium production is produced by remelting aluminium scrap.

1.2.2 Classification of aluminium alloys

From a materials perspective, aluminium alloys are commonly classified into wrought and cast alloys, depending on their processing route.

- Wrought aluminium alloys are originally cast as billets or ingots and then are processed through plastic deformation methods such as rolling, extrusion, or forging. These processes improve the strength, ductility and toughness of aluminium. Wrought aluminium typically requires low impurity levels and precise compositional control to ensure good mechanical performance and formability [19].
- Cast aluminium alloys are designed to be directly shaped from the liquid state by pouring the liquid aluminium into a mould in order to obtain the desired shape. Consequently, alloy fluidity, castability and resistance to solidification defects are crucial for cast aluminium [20]. From these characteristics, cast aluminium enables the production of more complex geometries and larger components, making it particularly suitable for the automotive and aerospace industries.

1.2.3 Aluminium-silicon (Al-Si) alloys

The most commonly used cast aluminium alloys in industrial applications are Al-Si alloys, aluminium containing Si as a major alloying element, due to their excellent castability and a desirable balance between mechanical properties (such as strength and toughness) and processability (such as fluidity, defect tolerance, and production cost). The addition of Si lowers the aluminium

melting temperature (Figure 1), increases melt fluidity, and reduces solidification shrinkage [21,22]. Also, Si addition improves the strength and hardness of the material by forming a eutectic Si phase within the α -aluminium matrix, which constrains plastic deformation and enhances wear resistance [23]. As a result, Al-Si alloys are being extensively used in both the aerospace and automotive industries [21].

The Al-Si alloys are divided into three areas based on Si concentration: hypoeutectic (Si content below 12.6 wt%), eutectic (Si content equal to 12.6 wt%), and hypereutectic (Si content above 12.6 wt%), as shown in the Al-Si phase diagram (Figure 1) [24]. Hypoeutectic and near-eutectic Al-Si alloys are widely used in both automotive applications due to their combination of good mechanical performance and manufacturing efficiency [23,25,26].

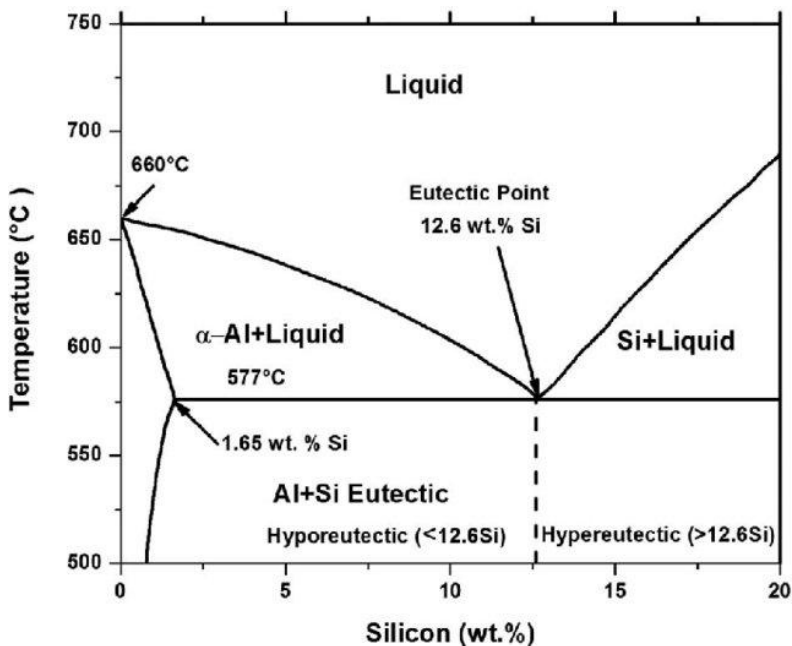


Figure 1. Al-Si phase diagram [24].

1.3 Sustainable aluminium production

1.3.1 Aluminium recycling

Due to its high strength-to-weight ratio, high corrosion resistance, and excellent electrical and thermal conductivity, aluminium has seen a significant increase in demand, leading to a significant expansion of primary aluminium production [1,2]. At the same time, the aluminium industry is facing increasing pressure to reduce the environmental impact of aluminium production, as primary aluminium production is energy-intensive and contributes significantly to global greenhouse gas emissions [3,4].

Consequently, future aluminium supply is expected to be driven by stricter environmental regulations and climate policies aimed at reducing greenhouse gas emissions in line with international agreements. In particular, the European Union has adopted a 2030 climate framework that aims to reduce greenhouse gas emissions by at least 55% relative to 1990 levels by 2030 [7]. This places intense pressure on energy-intensive industries, such as aluminium production, to reduce their carbon footprint.

One of the most effective ways to reduce the carbon footprint and the energy consumption of aluminium production is through aluminium recycling, as secondary aluminium production requires 90–95 % less energy and emits significantly lower CO₂ per kg of aluminium compared to primary aluminium production [5,6].

The circular economy is an industrial framework that has been increasingly adopted in recent years, aiming to close the loop by encompassing the design-manufacture-use-recycle cycle. This approach replaces the traditional linear economy method, the 'Take-Make-Dispose' production model, by minimising material waste and reintroducing end-of-life products as usable resources. Furthermore, the circular economy promotes both environmental sustainability and long-term economic development, particularly for energy-intensive production processes such as aluminium [27,28].

Figure 2 illustrates the life-cycle of aluminium production routes [29]. The top row of Figure 2 highlights the energy-intensive nature of primary aluminium

production (from both Bauxite refining and the electrolysis process), which is followed by product manufacturing and use. Recycling aluminium products after their service life enables partial closure of the materials loop (in line with the circular economy) by reducing the need for primary aluminium.

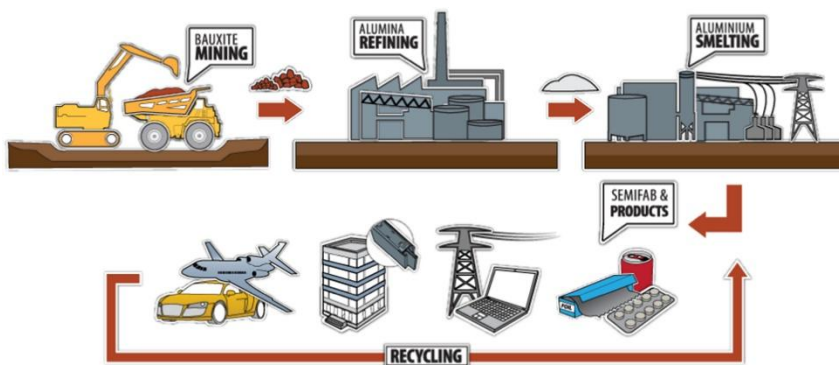


Figure 2. Aluminium life cycle, including the recycling loop [29].

1.3.2 Aluminium recycling limitation

The primary limitation of aluminium recycling is not the recycling itself but the progressive accumulation of impurities from mixed and downgraded scrap. Recycled aluminium has many more impurities and unwanted alloying elements that need to be reduced compared to primary aluminium [13]. Therefore, the quality and availability of scrap play a crucial role in recycling, as they vary greatly [3].

Impurities commonly present in recycled aluminium include, but are not limited to, dissolved gases, non-metallic solid inclusions, and dissolved impurities. Dissolved gases, particularly hydrogen, lead to porosity. Solid inclusions such as nitrides, bromides, carbides, chlorides and oxides cause undesirable defects when their content in the melt exceeds the critical point [30]. While dissolved impurities promote the formation of various intermetallic phases that reduce melt fluidity, increase porosity, and impair machinability, thereby negatively affecting the material's mechanical properties [8–10].

As a result, over the past 30 years, the demand for control and removal of impurities and aluminium cleanliness has increased [31]. High purity levels are also essential for many performance-critical applications in both the aerospace and automotive industries [32–34]. The high purity of aluminium positively influences its chemical and physical properties, such as conductivity, strength, and corrosion resistance. Many aluminium refining processes have therefore been developed and improved to be both environmentally friendly and cost-efficient.

1.3.3 Iron as a limiting impurity in Al-Si alloys

Iron (Fe) is widely regarded as one of the most detrimental impurities in aluminium alloys, particularly in Al-Si alloys, since Al-Si alloys constitute a large fraction of the recycled aluminium [27,35,36]. Fe is unavoidably introduced during the secondary aluminium production, originating from scrap streams and contamination from small steel components. Additionally, there is a lack of industrially viable refining processes for selectively removing dissolved Fe from the aluminium melt, resulting in progressive Fe accumulation with each recycling cycle [37].

High concentrations of Fe are problematic, as Fe forms the β -Al₅SiFe phase during the solidification of the molten aluminium alloy. The β -Al₅SiFe phase is characterised by a plate-like morphology with sharp edges, which significantly degrades both castability and mechanical performance of Al-Si cast alloys [13]. The coarse plate with sharp edges of the β -Al₅SiFe increases the stress concentration, leading to reduced ductility and increased susceptibility to crack initiation in aluminium alloys [13]. Also, the β -Al₅SiFe phase reduces feeding effectiveness, as Fe-bearing intermetallic particles block the melt and reduce its fluidity.

Figure 3a shows the morphology of the β -Al₅SiFe phase in the Al-Si microstructure, where the black flake-like phase is the eutectic silicon, the white phase is aluminium, and the grey plate-like phase is the β -Al₅SiFe phase (selected in Figure 3a). To illustrate the true three-dimensional morphology of the β -Al₅SiFe, a 3D reconstruction obtained by serial sectioning is presented in Figure 3b, where successive layers were mechanically polished, imaged and digitally stacked to recover the true 3D particle morphology [38].

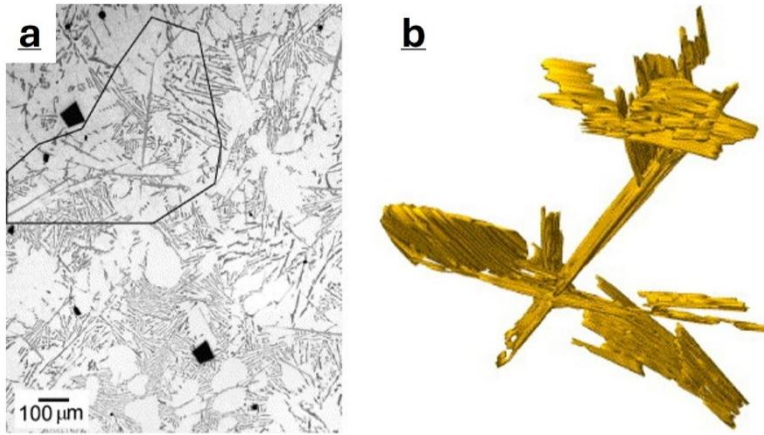


Figure 3. As-cast Al-Si alloy a. optical micrograph showing the plate-like β -Al₅SiFe particles b. 3D reconstruction of the β -Al₅SiFe obtained by serial sectioning [38].

1.4 Current strategies for Fe mitigation and their limitations

Based on the literature, a wide range of strategies has been investigated to mitigate the detrimental effects of Fe on Al-Si alloys. These methods can be broadly categorised into upstream control, melt treatment, and alloying strategies.

1.4.1 Upstream control: scrap sorting and dilution

The currently used industrial approach is scrap sorting and dilution of Al-Si alloys. In the scrap sorting stage, scrap streams are separated by alloy family to reduce compositional variability in the recycled aluminium streams. Currently, there are many effective and advanced sorting methods, such as Dynamic LIBS (laser-induced breakdown spectroscopy), X-ray transmission, and eddy current separation [39–41]. These sorting methods help mitigate the accumulation of Fe in recycled streams. However, Fe impurity cannot be completely eliminated by sorting alone, as it is present both as a contaminant and as an intentional alloying element in many aluminium products.

To achieve the Fe tolerance level of high-quality Al-Si alloys, the sorted scrap is diluted with low-Fe primary aluminium [6,42,43]. This strategy is simple and mostly used by secondary aluminium producers. This process is effective for processing high-quality scrap (low-impurity scrap). Primary aluminium dilution is not favourable since it diminishes both the environmental and economic benefits of aluminium recycling.

When considering low-quality scrap and high-purity aluminium (Fe content < 0.2 wt%), dilution becomes particularly impractical, as disproportionately large primary aluminium additions relative to the scrap mass would be required. Given the high energy consumption and carbon intensity of primary aluminium production, this approach progressively offsets the sustainability advantages of recycling [5,6,44].

1.4.2 Melt treatment techniques

The conventional melt treatment techniques for impurity removal in the aluminium industry are flux injections and filtration [1,45,46].

In the flux injection method, gas (nitrogen or argon) and metal powders (aluminium fluoride or magnesium chloride) are injected into the casting furnace to remove impurities from the aluminium melt [47]. These impurities will form slag and float to the surface when they react with the fluxing material [30,48]. The primary purpose of fluxing is to remove alkali metals (such as Na and Li) and oxide inclusions from the melt. However, the flux injection method has minimal effect on the Fe content in the melt.

For the filtration, a ceramic foam filter or a deep-bed filtration system is used to trap solid particles present in the melt. The efficiency of filtration depends strongly on particle size, morphology, and the timing of Fe-bearing intermetallic particle formation relative to the filtration step. This process is most effective when Fe-bearing intermetallic particles are large enough to get stuck in the mesh. However, in most Al-Si melts, Fe-bearing intermetallic particles precipitate during the solidification rather than in the fully liquid state (harder to filter) [49]. Moreover, the commonly formed β -Al₅SiFe phase exhibits a thin, plate-like structure, which conventional filtration methods may not effectively capture.

1.4.3 *Alternative purification techniques*

Alternative aluminium purification methods investigated for Fe removal include three-layer electrolysis, fractional crystallisation and vacuum distillation. These approaches mainly rely on the thermodynamic differences and volatility between aluminium and the Fe impurity.

Electrochemical processing is one of the most effective methods for removing impurities and obtaining high-purity aluminium [50,51]. In this method, an electric current is passed through the aluminium melt (enabling electrorefining). During electrolysis, aluminium is selectively deposited at the cathode, while many impurities (e.g., Fe) remain in the electrolyte, allowing Fe to be refined from molten aluminium. Some factories use three-stage electrolysis to further purify aluminium. In this method, the factories use three electrolytic cells and, in each layer, the aluminium is refined and purified further to reach the desired composition [50]. A significant disadvantage of this method is that it is expensive to run and has a negative environmental impact due to the high-power consumption it requires [50].

Fractional crystallisation is a purification method that exploits the differences in solubility of impurities in the material. During controlled solidification, aluminium-rich solid phases form first, while certain impurity elements are partitioned into the remaining liquid phase. The separation efficiency is determined by an equilibrium distribution coefficient, which is calculated as the ratio of the impurity concentration in the solid phase to that in the liquid phase [1,47]. For effective purification, the distribution coefficient should be significantly lower than 1 to ensure that the impurity segregates into the liquid phase during solidification, as is the case for Fe (0.018–0.053) [1,47].

The vacuum distillation method utilises differences in the physical properties of elements, namely their boiling points and vapour pressures. Under reduced pressure, elements with high vapour pressure evaporate and can be separated via condensation [33]. The effectiveness of the vacuum distillation mainly depends on the relative vapour pressure of aluminium and the target impurity. In the case of Fe, its vapour pressure is significantly lower than that of aluminium over typical processing temperatures, meaning aluminium would evaporate while Fe remains in the molten phase [33].

In theory, both fractional crystallisation and vacuum distillation could be used to reduce Fe in Al-Si alloys. However, the process's practical implementation is severely constrained by process complexity, high energy consumption, and substantial capital investment.

1.4.4 Alloying strategies

One of the best ways to mitigate the detrimental impact of the β -Al₅SiFe phase is by adding Fe-bearing intermetallic particle formers (sludge), like Mn and Cr, to the Al-Si alloy in order to transform the harmful β -Al₅SiFe phase into a less harmful α -phase [13–15,27,52–54]. This method helps reduce the impact of Fe and makes Fe-bearing intermetallic particles easier to remove without major changes to the current industrial setup, making it attractive to industry.

Song et al. [54] examined how Mn/Fe ratios influence Fe removal, as well as the impact of varying the initial Fe content on both the microstructure and mechanical properties of aluminium. Their results show that, in Al-7.0Si-2.4Fe alloy, increasing Mn/Fe ratio causes the primary Fe-rich phase to gradually shift from α -Al₈Fe₂Si to α -Al₁₅(Fe, Mn)₃Si₂. This phase transformation alters the morphology and stability of the Fe-bearing intermetallic particles, thereby improving overall removal efficiency.

According to Dietrich et al. [13], Mn promotes the formation of larger Fe-bearing intermetallic particles with higher particle density, thereby enhancing their gravitational settling and facilitating their easy removal by filtration or sedimentation. While Cr generates a greater number of smaller Fe-bearing intermetallic particles with lower density, making them harder to remove [13]. To overcome this limitation, a combination of Mn and Cr additions is often employed, as it promotes the formation of more and larger dendritic Fe-bearing intermetallic particles and, in turn, decreases the Fe content in the melt [13].

A paper by Mathew and Srirangam [55] also investigated the effect of the Mn-Sr combination on Fe-bearing intermetallic particles in Al-Si alloys. The results indicated that small amounts of Sr (0.04 wt%) slightly modify the Fe-bearing intermetallic particles. This study suggests that higher Mn-Sr ratios

may further modify the Fe-bearing intermetallic particles and influence Fe removal.

Several studies have demonstrated that varying the amounts of added Fe-bearing intermetallic particle formers in high-Fe Al-Si alloys significantly affects the morphology and characteristics of the particles [13,54,56]. Research conducted by Ferraro et al. [56] showed that in Al-9Si-3Cu(Fe) alloys, the formation kinetics, size distribution, and density of the Fe-bearing intermetallic particles are strongly influenced by the concentrations of Fe, Mn and Cr in the Al-Si alloys.

Furthermore, the amount of Fe-bearing intermetallic particles that is expected to form can be empirically predicted by calculating the sludge factor (SF) by using Equation 1, which relates the Fe-bearing intermetallic particles to the composition of Fe, Mn and Cr of the original alloy, expressed in wt% (w_x) [13]. The equation shows that Cr has a stronger contribution to the formation of Fe-bearing intermetallic particles than Mn. Additionally, the higher the value, the more easily the Fe-bearing intermetallic particles form. However, the SF is purely composition-based and ignores the kinetic factors, such as cooling rate, that may significantly affect the formation and growth of Fe-bearing intermetallic particles.

$$SF = w_{Fe} + 2w_{Mn} + 3w_{Cr} \quad 1$$

The melt-cooling rate and melt-holding temperature play a crucial role in the formation of Fe-bearing intermetallic particles, as demonstrated by Sanchez et al. [27]. The paper showed that lower holding temperature and slower cooling rate lead to improved Fe removal [27]. Longer cooling times and a hold temperature between the solidus and liquidus help promote polyhedral crystallite growth by providing time for particles to nucleate and grow. While shorter cooling times reduce the formation of large primary crystallites, which in turn reduces Fe removal efficiency [13], emphasising the strong relationship between thermodynamic driving forces and kinetic constraints during particle formation and growth.

In addition to the experimental investigation, Sinha et al. [57] developed a thermodynamic and kinetic model to describe the sedimentation behaviour of Fe-bearing intermetallic particles. In their work, the sedimentation velocity was derived using Stokes' law, indicating that the particles' settling behaviour depends primarily on particle diameter, the density difference between the particles and the liquid aluminium, and the melt viscosity. This model confirmed that as the particle size increases, the particles will settle faster. However, the model did not incorporate the particle growth during sedimentation.

After the Fe-bearing intermetallic particles have been created, they need to be removed by adding a further step, such as gravity separation, filtration, or electromagnetic (EM) separation.

- Gravity Separation: The aluminium melt is left undisturbed for an extended period for the Fe-bearing intermetallic particles to settle. The longer the settling time and the lower the temperature, the more Fe is removed from the metal [52,58,59].
- Filtration: Primary Fe-rich particles are eliminated using porous filters. In this process, the melt is held at the formation temperature of the Fe-bearing intermetallic particles. The melt is then decanted through a preheated filter to remove the formed Fe-bearing intermetallic particles [13,60].
- Electromagnetic (EM) separation: Applies an external magnetic field to the molten aluminium to generate forces within the electrically conductive molten aluminium. These forces help move and separate the Fe-bearing intermetallic particles from the melt due to differences in their physical properties (between Fe and aluminium) [61–63].

1.5 Knowledge gap

Recycled aluminium reliance has significantly increased to reduce the carbon footprint and energy consumption. Therefore, significant advances in aluminium refining technologies have been made, particularly in refining Fe impurities. Among the current Fe removal methods, one of the most

industrially applicable approach, given current technologies' readiness levels, is the addition of Fe-bearing intermetallic particle formers. This method helps reduce the impact of Fe. Also, this method makes the Fe-bearing intermetallic particles easier to handle and dispose of, with minimal changes to the current industrial setup and at minimal cost.

Although Fe mitigation in Al-Si alloys via alloy addition has been extensively researched, most studies focus on alloys with relatively high Fe contents (0.8–2 wt%) [13–15,27,52–54]. However, limited research has been conducted to investigate the Fe removal efficiency and particle characteristics of Al-Si alloys with low initial Fe content. The available findings for high initial Fe content cannot be extrapolated, as the primary Fe-rich phase, including thermodynamic driving forces, particle population, and separation efficiency, may differ. Also, limited research has been conducted on different Fe-bearing intermetallic particle formers, such as strontium (Sr), in combination with Mn.

Additionally, there is a lack of validated models, correlated with experimental data, that couple particle growth, sedimentation kinetics and morphology-dependent resistance across different cooling rates. Such an integrated approach is necessary to better understand the dynamic behaviour of the Fe-bearing intermetallic particles in the melt and to determine the required holding time prior to solidification or particle removal to obtain the optimal clean yield.

1.5.1 Research focus

Based on the identified knowledge gaps, the main aim of the research is to develop a deeper quantitative understanding of Fe removal in low-Fe Al-Si alloys by investigating the formation and sedimentation behaviour of Fe-bearing intermetallic particles under different Mn, Cr, and Sr combinations. Also, this research seeks to establish a scientifically grounded, process-relevant framework to define the governing physical and kinetic constraints of particle sedimentation on Fe removal, thereby supporting more reliable process control. Ultimately, these findings contribute to reducing reliance on primary aluminium dilution within the existing industrial setup.

2 Research Approach

Chapter introduction

This chapter presents the research purpose and outlines the methodological framework adopted for this work. Additionally, the main experimental and modelling procedures used to address the research questions are summarised.

2.1 Purpose and aim of the research

The main aim of this research is to make aluminium production resource-efficient, climate-neutral, and circular by improving the separation of unwanted impurities from recycled aluminium. The primary focus of this research is the effective removal of Fe in secondary Al-Si alloys, as Fe accumulation remains a critical limitation in the recycling of Al-Si alloys.

This thesis investigates Fe refining through the formation and sedimentation of Fe-bearing intermetallic particles in low-Fe Al-Si alloys. By systematically evaluating the influence of alloying additions and solidification conditions, the research aims to provide industrial partners with scientifically valuable information and calculation tools that support the industrial production of aluminium with improved Fe removal efficiency and reduced environmental impact.

2.1.1 Reflection on the chosen method

An experimental approach method based on deductive reasoning, assisted by equilibrium calculations using Thermo-Calc software [64], was employed in this research. The experiments were carried out on a well-controlled laboratory scale, with each experiment isolated and only certain controlled parameters varied at a time. This was done to improve the precision of the experiments that were performed. Also, when possible, ISO standards were

followed during sampling and testing. To enhance the validity, reliability, and reproducibility of the findings, multiple iterations of the analysis were conducted for each sample.

2.2 Research design

2.2.1 *Research perspective*

This research employs a positivistic approach methodology anchored in deductive reasoning principles to identify clear causal-and-effect relationships among independent and dependent variables in the performed experiments. In deductive reasoning, the tested hypothesis could either be accepted or rejected after examining the quantitative and experimental results [65,66]. Deductive research includes the following steps:

1. Formulate a hypothesis and research questions.
2. Plan the study (research design, chosen sample population and data collection method).
3. Gather data.
4. Analyse the data.
5. Draw conclusions.

The conclusions are based on the analysed data, which either corroborate or refute the hypothesis and could provide insights for future studies.

2.2.2 *Research methodology*

This research project primarily involves theoretical and experimental research in a laboratory setting. The investigation was initiated by identifying the main refining problems and challenges currently faced by the aluminium recycling industry. After that, a focused, comprehensive literature review was conducted to establish the scientific background and identify knowledge gaps related to the formation and sedimentation of Fe-bearing intermetallic

particles in low-Fe Al-Si alloys. After identifying a research gap, the research questions were formulated accordingly.

The experimental setup was designed, and pre-experiments were conducted to test it and verify new procedures, ensuring controlled, reproducible conditions. Then, a series of controlled small-scale experiments was conducted, followed by systematic evaluation and analysis of the results.

This research will be divided into two areas: sample manufacturing and sample analysis. Sample analysis includes composition analysis and microstructure characterisation. In the end, the collected data were analysed to establish relationships between alloy composition, Fe-bearing intermetallic particle formation and sedimentation, and Fe removal behaviour. An overview of the research methodology is shown in Figure 4.

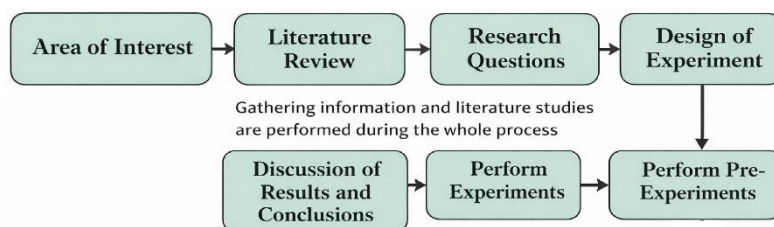


Figure 4. Overview of the research methodology.

2.2.3 Research questions

Based on both the industrial needs and the current research gaps regarding Fe removal in low-Fe Al-Si alloys, the presented research is guided by the following research questions:

RQ1

How does alloy chemistry, particularly Mn, Cr and Sr additions, influence the formation, population and morphology of the Fe-bearing intermetallic particles in low Fe-Al-Si alloys? (Supplements I and II)

Targeted knowledge gap: Limited research has been conducted to investigate the effects of Mn and Mn-Cr additions on the

characteristics of Fe-bearing intermetallic particles in low-Fe Al-Si alloys. Also, limited research has been conducted on different Fe-bearing intermetallic particle formers, such as strontium (Sr), in combination with Mn.

RQ2

To what extent could the Fe removal in low-Fe Al-Si melt be enhanced through Fe-bearing intermetallic particle former additions, and what trade-offs could arise? (Supplements I and II)

Targeted knowledge gap: Limited research has been conducted to investigate the Fe removal efficiency and potential trade-offs of Al-Si alloys with low initial Fe content. Also, limited research has been conducted on different Fe-bearing intermetallic particle formers, such as strontium (Sr), in combination with Mn.

RQ3

How do the cooling rate and particle morphology affect growth, interactions and sedimentation behaviour of the Fe-bearing intermetallic particles? (Supplement III)

Targeted knowledge gap: There is a lack of validated models, correlated with experimental data, that couple particle growth, sedimentation kinetics and morphology-dependent resistance across different cooling rates. Such an integrated approach is necessary to better understand the dynamic behaviour of the Fe-bearing intermetallic particles in the melt. It also helps determine the required holding time before solidification or particle removal to achieve the optimal clean yield.

Following the formation of the research questions, their relation to each appended paper and the overall thesis framework is illustrated in Figure 5.

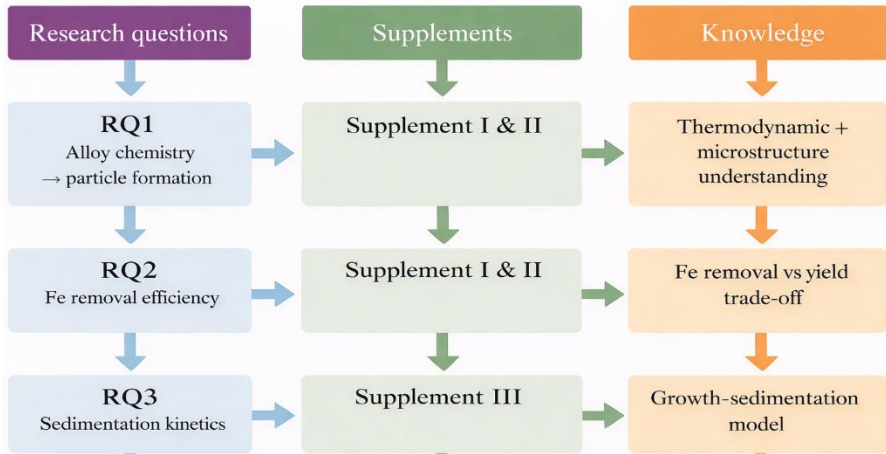


Figure 5. Schematic illustration of the research questions' relation to Supplements I, II and III.

2.3 Material and experimental procedures

The experimental procedure that was conducted in this research is summarised in Figure 6. This thesis starts with Thermo-Calc calculations to define the amounts of Mn and Cr additions for each experiment and the temperature ranges for sampling. Based on these calculations, 8 kg of the used Al-Si alloy was melted, and the master alloys to increase the Mn, Cr, and Sr were added. After the master alloys had dissolved, two types of samples were collected: the Fe-bearing intermetallic particle analysis samples and the chemical analysis samples.

The Fe-bearing analysis samples were examined using optical and scanning electron microscopy in order to characterise the Fe-bearing intermetallic particles' morphology, sedimentation rate and packing density.

The chemical analysis samples were analysed by optical emission spectroscopy to monitor the melt composition as temperature decreased and to determine the Fe removal efficiency.

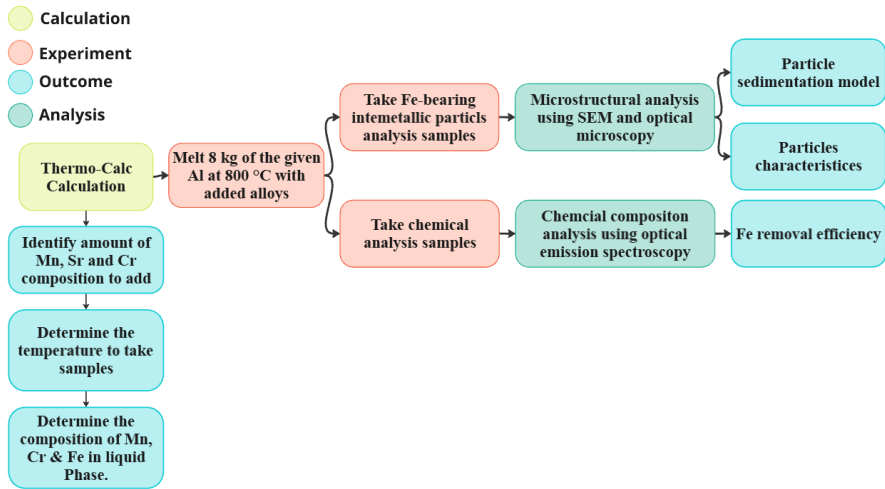


Figure 6. Schematic illustration of the experimental procedure performed for Supplements I, II and III.

2.3.1 Alloys

In all the Supplements, EN-AB 44300 secondary cast aluminium alloy was the base alloy used. The composition of the base alloy, obtained using the optical emission spectroscopy (OES, SPECTROMAXx CCD LMXM3, AMETEK), is shown in Table 1.

Table 1 Chemical composition of the EN-AB 44300 base alloy.

Alloy	(wt%)	Si	Fe	Mn	Cr	Sr	Al
EN-AB 44300	Avg	11.0	0.51	0.11	0.01	0.01	Bal
	Std	0.2	0.01	0.01	0.001	0.001	-

Fe-bearing intermetallic particle formers, including Mn, Cr and Sr, were introduced individually or in combination, depending on the specific study. For Mn and Cr additions, the composition ranges were selected based on the thermodynamic equilibrium calculations performed using Thermo-Calc (TCAL8/Al-alloys database version 8.2) [64]. The lowest Mn and Cr compositions were selected at the point where the Al15Si2M4 phase becomes

the stable primary precipitation phase and remains stable until complete solidification. The highest Mn and Cr composition was selected at the point where Al₁₅Si₂Mn₄ forms without the nucleation of other phases.

That is not the case for Sr addition, since the effect of Sr on the Fe-bearing intermetallic particles is not represented in the Thermo-Calc database used. Therefore, the Sr content was chosen empirically, with relatively high additions used to amplify the Sr effect on the morphology and packing density of the Fe-bearing intermetallic particles [67,68].

2.3.2 Sample preparation

In Supplements I, II and III, a series of small-scale experiments were performed. In each experiment, 8 kg of recycled EN-AB 44300 alloy was melted at 750 °C in a tilting furnace. Seven different experiments were conducted using different Mn, Cr and Sr combinations. In order to reach the desired composition, master alloys were used (Al-80Mn, Al-10Cr and Al-20Sr).

The sample production is divided into two parts: the Fe-bearing intermetallic particle analysis and the chemical analysis samples.

In the Fe-bearing intermetallic particle analysis samples, the melt was poured into two preheated steel moulds (preheated to 900 °C). The preheated mould was submerged in the melt, and the two samples were taken. Then, the moulds were covered. One mould was covered (insulated) with 1 cm-thick alumina (Al₂O₃) wool, and the other mould was covered (insulated) with a 1 cm-thick cylindrical steel cover. The temperature was then measured with a K-type thermocouple. The cooling rate of the melt in the alumina-wool-covered sample was 30 °C/min, and in the steel-covered sample was 84 °C/min. The schematic representation of the setup is shown in Figure 7. These samples were used in Supplements II and III.

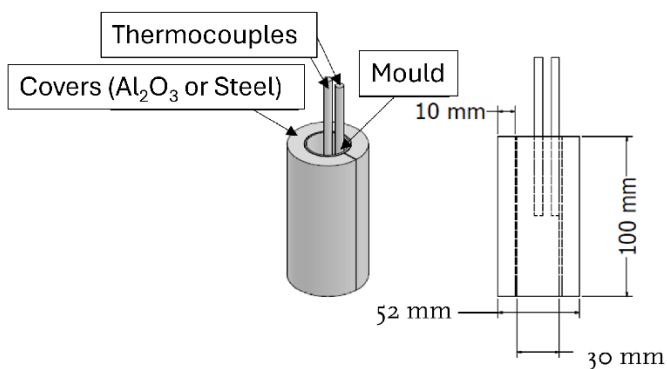


Figure 7. Schematic illustration of the Fe-bearing intermetallic particle analysis sample setup.

The remaining melt in the furnace was then cooled at 3 °C/min. During the cooling stage, two to three samples were taken at temperatures above the formation temperature of the Fe-bearing intermetallic particles. This formation temperature was determined by Thermo-Calc. In Thermo-Calc, the Al₁₅Si₂M₄ phase, where M is a combination of Fe, Mn, and Cr, is the term used to describe the Fe-bearing intermetallic phase. Then, four to five samples were taken at temperatures below the Al₁₅Si₂M₄ formation temperature.

In the Sr addition case, to ensure direct comparability and eliminate temperature as a variable, samples were taken at the same temperatures as for the 1.2Mn0.3Cr alloy addition, as the two alloys are compared in Supplement II.

All samples were taken from the top of the crucible (0.2 m height × 0.25 m diameter) to evaluate the Fe concentration in the particle-depleted zone following sedimentation. The melt was poured into a coin-shaped copper mould using a scoop to ensure rapid solidification and minimise post-sampling microstructural evolution. The schematic representation of the mould's geometry is shown in Figure 8. These samples are hereafter referred to as the chemical analysis samples and were used in Supplements I and II.

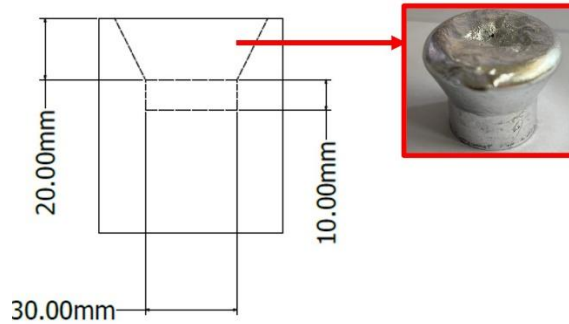


Figure 8. Schematic illustration of the chemical analysis sample setup.

2.3.3 Sample and alloy testing

The chemical analysis samples used in Supplements I and II were analysed by optical emission spectroscopy (OES) to determine the melt's chemical composition at different temperatures during furnace cooling. For each sample, four OES measurements were taken at different locations and averaged to improve the statistical reliability of the composition by minimising the influence of local microsegregations and spark-to-spark variability.

Before measuring the composition of the samples, certified reference materials (CRMs) were analysed (using OES) to validate the instrument's calibration and ensure analytical accuracy.

2.3.4 Material characterisation and evaluation

Before particle characterisation, the samples were metallographically prepared. These preparations include the longitudinal cutting, grinding and polishing of the Fe-bearing intermetallic particle analysis samples as shown in Figure 9.

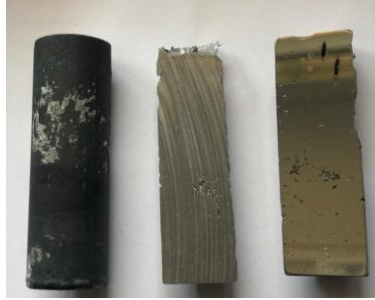


Figure 9. Metallographic preparation of the Fe-bearing intermetallic particle analysis sample.

Then, the chemical composition of the particles in the micrograph was investigated using scanning electron microscopy (SEM, Tescan LYRA3) and energy-dispersive X-ray spectroscopy (EDS, EDAX Octane Plus) to identify and quantify the composition of the Fe-bearing intermetallic particles. Particles containing Mn, Cr, Fe and Si in their composition were identified as Fe-bearing intermetallic particles.

The microstructures of the samples were then studied using a DSX1000 optical microscope. A panoramic view of the entire sample was taken to identify the sedimented region and measure its height. The sedimented region is the region in which the Fe-bearing intermetallic particles have settled at the bottom of the sample (since they are denser than the aluminium melt).

A magnified panorama image of a small section of the sedimented region ($1018 \mu\text{m} \times 2036 \mu\text{m}$) was acquired to perform quantitative image analysis of the Fe-bearing intermetallic particles using MIPAR software. This was done to obtain the total area fraction and the total number of Fe-bearing intermetallic particles in the sedimented region (Supplements II and III).

2.3.5 Modelling methodology

To further evaluate the sedimentation behaviour of Fe-bearing intermetallic particles, a physics-based particle growth and sedimentation model was developed.

This was done by integrating the growth kinetics of Fe-bearing intermetallic particles with settling velocity calculations derived from the force balance, since simple Stokes' law was insufficient to describe the settling behaviour of growing particles. The calibration of this model was performed using experimental measurements of sedimented height, max particle height and the area fraction of the sedimented Fe-bearing intermetallic particles at different cooling rates.

3 Results and Discussion

Chapter introduction

This chapter focuses on the critical results and discussion for the appended papers.

3.1 Equilibrium and experimental chemical analysis of alloy addition on Fe removal

3.1.1 *Equilibrium calculation*

Based on the literature review, the formation of Fe-bearing intermetallic particles in low-Fe Al-Si alloys is mainly governed by alloy chemistry, which determines the tendency of the Fe-bearing intermetallic phase to form at a given temperature and composition. The thermodynamic equilibrium stability was predicted using Thermo-Calc, including the phase formation temperature and the equilibrium volume fraction of the Fe-bearing intermetallic particles. The Al₁₅Si₂M₄ phase is the term that Thermo-Calc used to describe the Fe-bearing intermetallic phase.

Based on Supplement I, the thermodynamic equilibrium analysis showed that increasing the Mn content from 0.6 to 1.5 wt% in low-Fe Al-Si alloys stabilises the Al₁₅Si₂M₄ phase at higher temperatures (increases formation temperature by 50 °C) and increases the particle volume fraction from 2.4 % to 5.7 %. This implies an increase in thermodynamic driving force for the Fe partitioning from the aluminium melt into the Al₁₅Si₂M₄ phase.

When Cr is introduced alongside Mn (Supplement II), the formation temperature of the Al₁₅Si₂M₄ phase increases significantly compared to the Mn-only addition. In the 0.6Mn case, the addition of 0.6 wt% of Cr shifts the formation temperature from 600 to 735 °C. In contrast, when increasing the Mn content to 1.5 wt% with the same Cr addition, the formation temperature

only increases by 4 °C. This behaviour indicates that Cr addition has a more dominant influence on increasing the Al₁₅Si₂M₄ phase formation temperature. In contrast, an increase in Mn addition has a weaker impact on the formation temperature.

Mn addition strongly affects the particle equilibrium volume fraction in low-Fe Al-Si alloy. Increasing Mn from 0.6 to 1.5 wt% at constant 0.6 wt% of Cr significantly increases the equilibrium volume percent of the Al₁₅Si₂M₄ phase from 3.1 % to 5.9 %.

When looking into Sr addition in combination with Mn (Supplement II), the Sr addition does not alter the calculated equilibrium formation temperature of the Fe-bearing intermetallic particles. This is due to the fact that the ThermoCalc database (TCAL8.2) used does not account for the effect of Sr in the formation of the Fe-bearing intermetallic particles.

3.1.2 Chemical analysis

The equilibrium calculations helped define the maximum achievable Fe removal (under ideal conditions). However, they don't account for the precipitation of non-equilibrium phases and time-dependent kinetic factors, such as nucleation rates, diffusion-controlled growth, and sedimentation dynamics. Therefore, OES measurements were performed on the chemical analysis samples for all seven cases to monitor the Fe reduction as a function of temperature. The results of Fe content as a function of temperature are shown in Figure 10 (Supplements I and II).

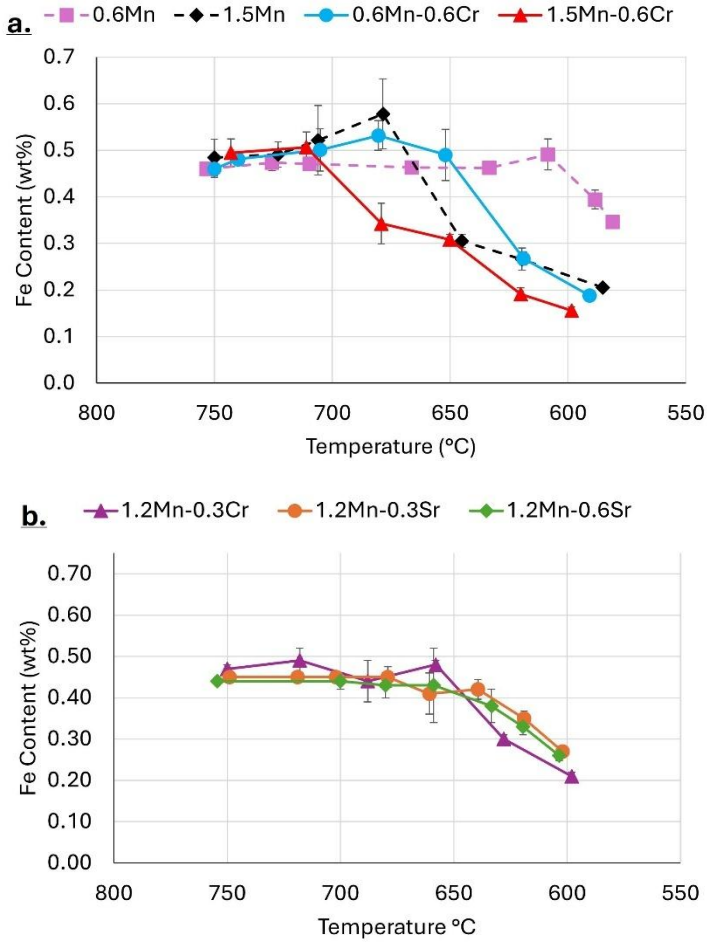


Figure 10. Experimentally obtained Fe composition, using OES, as a function of temperature for a. 0.6Mn, 1.5Mn, 0.6Mn0.6Cr and 1.5Mn0.6Cr b. 1.2Mn0.3Cr, 1.2Mn0.3Sr and 1.2Mn0.6Sr.

The Fe removal efficiency (η) was then calculated using Equation 2 for all seven cases.

$$\eta = \frac{C_{\text{initial}} - C_{\text{final}}}{C_{\text{initial}}} \times 100 \quad 2$$

Where C_{initial} and C_{final} represent the Fe content in the melt at the beginning (prior to intermetallic formation) and at the end of the experiment (last taken chemical analysis sample), respectively. The results are summarised in Tables 2 and 3.

Table 2 Fe removal efficiency of 0.6Mn, 1.5Mn, 0.6Mn0.6Cr and 1.5Mn0.6Cr.

Alloy	0.6Mn	1.5Mn	0.6Mn0.6Cr	1.5Mn0.6Cr
Fe removal efficiency (%)	26	56	59	69

Table 3 Fe removal efficiency of 1.2Mn0.3Cr, 1.2Mn0.3Sr and 1.2Mn0.6Sr.

Alloy	1.2Mn0.3Cr	1.2Mn0.3Sr	1.2Mn0.6Sr
Fe removal efficiency (%)	55	40	41

In the Mn additions (Supplement I), increasing the Mn content (dashed lines in Figure 10a) from 0.6 to 1.5 wt% significantly improves the Fe removal efficiency (Table 2) and shifts the onset of Fe reduction to a higher temperature (from 610 to 706 °C). This indicates that increasing the Mn content promotes the earlier formation of Fe-bearing intermetallic particles and enhances the driving force for Fe partitioning in low-Fe Al-Si alloys (Supplement I).

The addition of Cr in combination with Mn (Supplement II) further improves the Fe removal compared to Mn addition (Supplement I), as shown in Figure 10a and Table 2. In addition to increasing the Fe removal efficiency, Cr addition shifts the onset temperature significantly (meaning Fe starts to decrease at higher temperatures). This increase in the onset temperature extends the available time window for particle growth and sedimentation, thereby benefiting Fe removal in low-Fe Al-Si alloys.

A Fe removal comparison between Mn-Cr and Mn-Sr at constant Mn is shown in Figure 10b and Table 3 (Supplement II). The results show that Mn-Cr addition is more effective than Mn-Sr addition for Fe removal, while both

exhibit similar onset temperatures. When Sr is further increased from 0.3 to 0.6 wt%, the Fe removal efficiency increases slightly, and the onset temperature remains the same (within experimental uncertainty). This means that a further increase in Sr has a limited effect on Fe removal in low-Fe Al-Si alloys.

The details of how combinations of Mn, Cr, and Sr additions influence Fe removal efficiency will be discussed in later sections (Section 3.2).

3.1.3 Chemical analysis vs equilibrium calculation

To better understand how Mn, Cr, and Sr influence Fe removal and to evaluate how closely the experimental results match Thermo-Calc equilibrium calculations, the latter were compared with the OES composition results obtained in the experiment.

Supplement II compared the experimental data with the equilibrium data of both 0.6Mn0.6Cr and 1.5Mn0.6Cr. The results are shown in Figure 11.

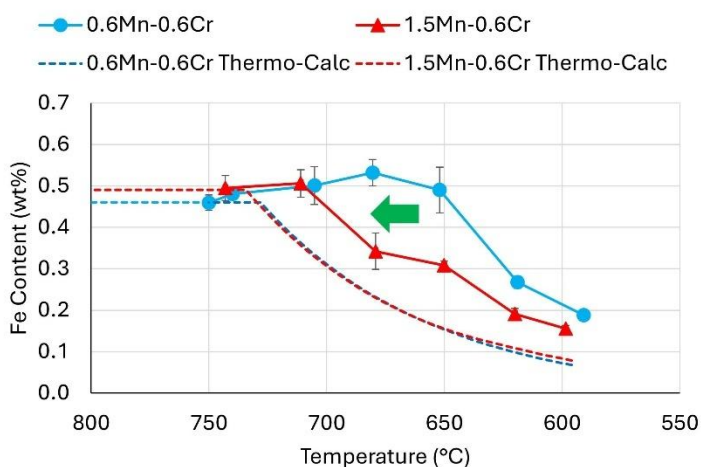


Figure 11. Measured Fe compositions against temperature for 1.5Mn0.6Cr and 0.6Mn0.6Cr alloys, showing experimental and equilibrium data, and the green arrow shows the shift of the experimental data towards equilibrium.

Under equilibrium conditions and constant Cr, increasing Mn from 0.6 wt% to 1.5 wt% results in only minor differences in the equilibrium Fe content in the liquid as temperature decreases. However, equilibrium predictions and comparisons with experimental data indicate that the Fe concentration measured by OES remains higher than the corresponding equilibrium values.

Furthermore, increasing the initial Mn content significantly enhances Fe removal efficiency, bringing the measured Fe content closer to equilibrium predictions (green arrow in Figure 11). This behaviour indicates that increasing the initial Mn content accelerates the formation kinetics and promotes faster sedimentation of the Fe-bearing intermetallic particles during cooling.

To support this interpretation, microstructural analysis was conducted on the four chemical analysis samples collected at different stages of cooling. The chosen samples are: (i) the sample taken at the highest temperature, (ii) the sample collected immediately before the onset of Fe decrease, (iii) the sample collected shortly after Fe reduction and (iv) the sample taken at the lowest temperature. The representative micrograph and area fraction (f_p) of all four chemical analysis samples are shown in Figure 12 (Supplement II). The dark grey in the micrographs is the Fe-bearing intermetallic particles.

The micrographs and the Fe-bearing intermetallic particles area fraction analysis help explain why the measured experimental Fe content is higher than the predicted equilibrium Fe content. One reason is that the OES results obtained from the chemical analysis samples included both suspended Fe-bearing intermetallic particles and the liquid metal. While the equilibrium Fe content is the content of the liquid melt only. Although part of the discrepancy between the experimental and equilibrium Fe content can be attributed to suspended intermetallic particles in the sampled melt, this does not fully account for the difference.

When looking at lower temperatures (590–600 °C), most of the Fe-bearing intermetallic particles have settled (indicated by low f_p), and there is still a significant difference between the equilibrium and experimental results. This indicates that thermodynamic equilibrium was not reached during cooling,

most likely due to kinetic limitations associated with nucleation, growth and sedimentation dynamics of the Fe-bearing intermetallic particles.

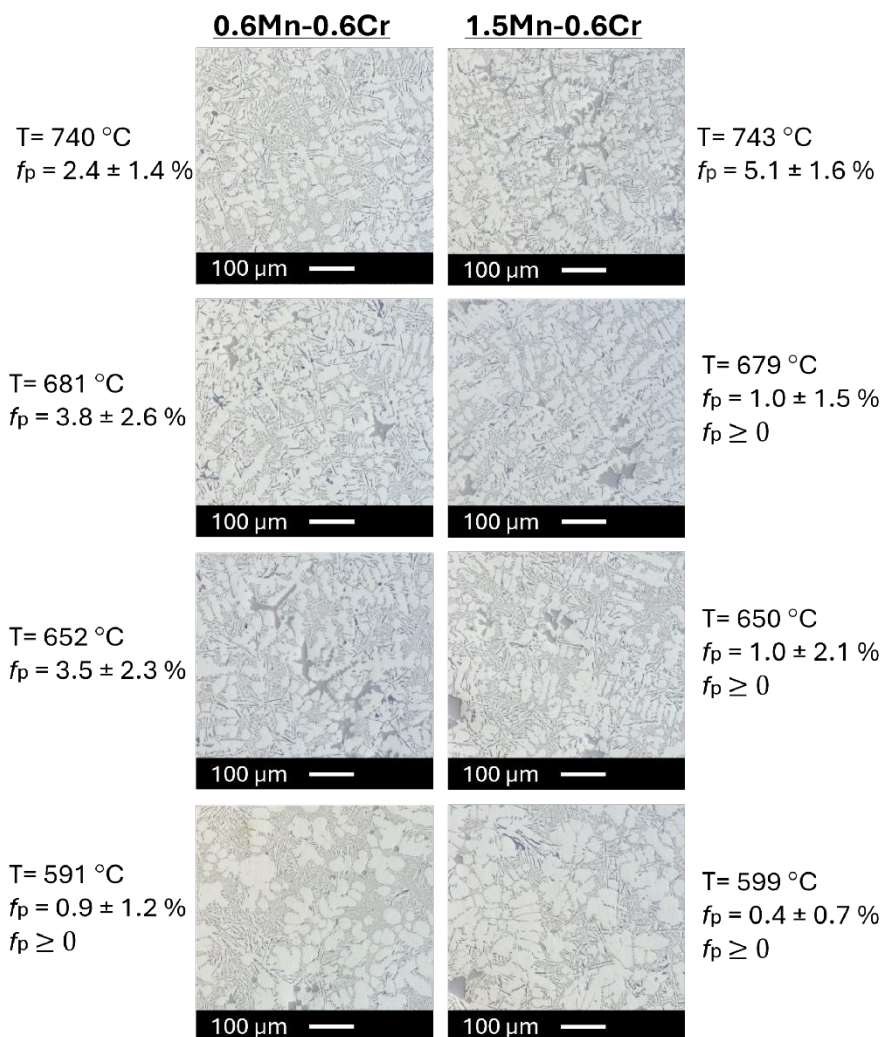


Figure 12. The micrographs, along with the area fraction of the Fe-bearing intermetallic particles (f_p) of four chemical analysis samples at different temperatures for 0.6Mn0.6Cr and 1.5Mn0.6Cr alloys.

The comparison of equilibrium and experimental Fe content performed in Supplement II for 0.6Mn0.6Cr and 1.5Mn0.6Cr was also performed for 0.6Mn

and 1.5Mn (Figure 13). Figure 13 shows that the Fe content obtained from the sample analysis is lower than the equilibrium. These deviations suggest the precipitation of non-equilibrium Fe-rich intermetallic phases during cooling. Although equilibrium calculations predict the Al₁₅Si₂M₄ phase as the primary phase, experiments performed by Que et al. [69] show that θ -Al₁₃Fe₄ and Al₆(Fe, Mn) nucleate under experimental conditions. This means that intermetallic phases, which are not accounted for in equilibrium calculations, further reduce the Fe content of the melt. As a result, the experimental Fe content is lower than the equilibrium value.

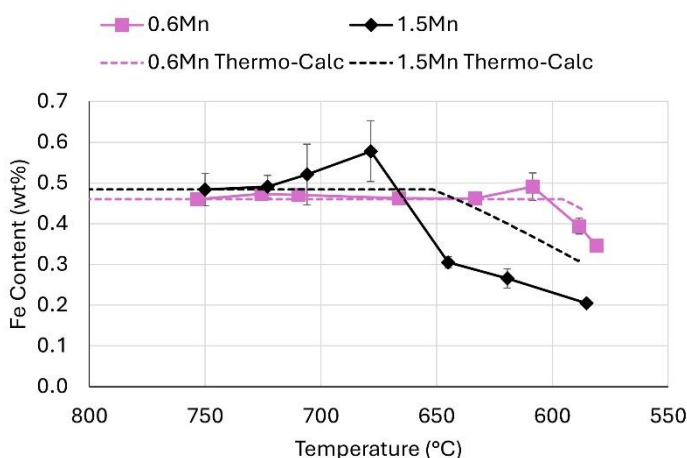


Figure 13. Measured Fe compositions against temperature for 0.6Mn and 1.5Mn alloys, showing experimental and equilibrium data.

3.2 Microstructural evaluation of Fe-bearing intermetallic under different alloy additions

The deviations between experimental and equilibrium Fe content (discussed in Section 3.1) demonstrate that the Fe removal is governed not only by thermodynamic stability but also by kinetic processes. In particular, particle nucleation, diffusion-controlled growth, and sedimentation dynamics determine how effectively the thermodynamic driving force is realised during cooling in the 0.6Mn0.6Cr and 1.5Mn0.6Cr cases.

For the remaining alloy additions (0.6Mn, 1.5Mn, 1.2Mn0.3Cr, 1.2Mn0.3Sr, and 1.2Mn0.6Sr), equilibrium calculations were not helpful because the Thermo-Calc database used here has limitations. Therefore, equilibrium analysis alone is insufficient to explain the decrease in Fe in these additions.

To understand how and why the Fe content in the melt decreases, direct examination of the evolution of Fe-bearing intermetallic particles during cooling is necessary. Accordingly, this section analyses the microstructural development of the Fe-bearing intermetallic particles and evaluates how different alloy additions and their combinations influence the particle population, morphology, and sedimentation behaviour. The Fe-bearing intermetallic particle analysis samples were used to investigate the Fe-bearing intermetallic particles in each alloy addition.

The slow-cooling (alumina-covered) Fe-bearing intermetallic particle analysis samples were selected for detailed Fe-bearing intermetallic particle analysis because they provide a longer time for particle growth and sedimentation, while minimising kinetic undercooling effects.

Additionally, comparisons between experimental and equilibrium volume fraction of the Fe-bearing intermetallic particles show that, under slow-cooling conditions, the measured intermetallic particle volume fraction exceeds the predicted equilibrium volume fraction. Whereas under fast-cooling (Fe-covered samples), the experimental intermetallic particle volume fraction remains below the equilibrium values (Supplements II and III).

This behaviour indicates that the slow-cooling Fe-bearing intermetallic particle analysis samples provide a reliable reference for approximating the near-equilibrium growth path. Therefore, the slow-cooling samples were used as a more representative reference for investigating the influence of Fe-bearing intermetallic particles in each alloy addition.

A panorama image of the full slow-cooled Fe-bearing intermetallic particle analysis sample and a 1 mm × 2 mm micrograph image in the sedimented area of the Fe-bearing were taken. From the panorama image, the aluminium clean yield was calculated using Equation 3. The sedimentation height is described using two parameters. The first parameter, h_{sed} , represents the height of the particles that have settled to the bottom of the mould. The second parameter,

h_{max} , is the maximum height of the sedimented particle that did not reach the settled region before the solidification. In Equation 3, h_{max} was used to calculate the yield since the yield is calculated from the fraction of the sample height that does not contain any particles.

$$\text{Yield} = \left(1 - \frac{h_{max}}{h_{total}}\right) \times 100 \quad 3$$

Where h_{total} is the total height of the sample (0.1 m). Then, from the micrograph of the sedimented region, the elemental composition and packing density of the Fe-bearing intermetallic particles were determined using MIPAR and EDS, respectively. The packing density is defined as the level of compactness of the Fe-bearing intermetallic particles in the sedimented region of the sample. In these cases, the packing density is assumed to be equal to the Fe-bearing intermetallic particles area fraction, as the micrograph is bidimensional and can be easily evaluated.

3.2.1 Comparison between Mn-only and Mn-Cr additions

The results of the yield calculation (Equation 3), packing density and elemental composition are summarised in Table 4. For the 0.6Mn addition case, no settled layer was observed. According to Thermo-Calc, the Fe-bearing intermetallic particles are only just becoming thermodynamically stable as a primary phase; i.e., the volume (number) of Fe-bearing intermetallic particles is nearly zero. Thus, the yield, packing density, and composition of the particles were not calculated.

Table 4 Summary of particles' yield, packing density and elemental composition of Fe-bearing intermetallic particle analysis sample in 1.5Mn, 0.6Mn0.6Cr and 1.5Mn0.6Cr alloys.

Alloy	Yield (%)	Packing Density (%)	Intermetallic Particles Composition (wt%)		
			Fe	Mn	Cr
1.5Mn	85	10.1 ± 1.4	7.8 ± 0.5	21.7 ± 0.8	-
0.6Mn0.6Cr	55	6.4 ± 1.3	7.9 ± 0.2	9.2 ± 0.2	10.9 ± 0.3
1.5Mn0.6Cr	42	12.8 ± 1.4	5.6 ± 0.3	15.4 ± 0.8	7.5 ± 0.4

The results reveal that when Mn is increased at constant Cr, the Fe and Cr content of the Fe-bearing intermetallic particle decreases while the Mn content significantly increases. This indicates competitive partitioning between Mn and Cr. This means that increasing the Mn content in the melt promotes the formation of Mn-rich Fe-bearing intermetallic particles. The same trend is observed for Mn-only addition; the Fe content in the particle decreases and the Mn content increases as the Mn addition increases, as shown in Supplement I.

Overall, increasing Mn addition leads to a shift in the intermetallic chemistry towards Mn-rich Fe-bearing intermetallic particles and reduces both Fe and Cr incorporation.

Regarding yield and particle packing density, the Mn-only addition in a low-Fe Al-Si alloy yields the highest clean aluminium. While the Mn-Cr combination leads to a significant reduction in the yield, which is mainly attributed to the formation of more dendritic Fe-bearing intermetallic particles [56]. Furthermore, the 1.5Mn0.6Cr addition shows a slight increase in the packing density compared to the 1.5Mn addition.

Since Fe removal occurs through nucleation, growth and sedimentation of the Fe-bearing intermetallic particles, both their composition and the sedimented fraction directly influence the overall Fe removal efficiency.

In order to better quantify the contribution of the Fe-bearing intermetallic particles and the removal efficiency, the Fe removal potential (ϕ_{Fe}) was calculated using Equation 4.

$$\phi_{\text{Fe}} = \left(\frac{PD}{100} \times \frac{w_{\text{Fe,p}}}{100} \times \frac{\eta}{100} \right) \times 100 \quad 4$$

Where PD is the particle packing density, η is Fe removal efficiency and $w_{\text{Fe,p}}$ is the average Fe content in the Fe-bearing intermetallic particles.

In Supplement I, the Fe removal efficiency was not included in the Fe removal potential. The reason for this was that, at the stage of writing Supplement I, the analysis primarily focused on particle chemistry and packing density, which describe the capacity of the intermetallic phase to capture Fe. However, the PD and the $w_{\text{Fe,p}}$ alone does not reflect how effectively Fe is removed from the melt, since it does not account for the actual fraction of Fe separated from the melt.

Therefore, the η is incorporated in the ϕ_{Fe} calculation to ensure that ϕ_{Fe} accounts for both the Fe stored within the particle and the effective Fe removal achieved during sedimentation. This provides a more realistic, process-relevant evaluation of Fe separation by linking microstructural characteristics and Fe removal efficiency. The results for ϕ_{Fe} are summarised in Table 5.

Table 5 Fe removal potential for 1.5Mn, 0.6Mn0.6Cr and 1.5Mn0.6Cr.

Alloy	Fe removal potential (%)
1.5Mn	0.44
0.6Mn0.6Cr	0.30
1.5Mn0.6Cr	0.50

The calculated ϕ_{Fe} indicates that 1.5Mn0.6Cr achieves the highest removal potential, and 0.6Mn0.6Cr has the lowest. However, this improvement in Fe removal potential in 1.5Mn0.6Cr comes at a significant reduction in the clean

aluminium yield (Table 4), highlighting a clear trade-off between Fe separation efficiency and melt recovery.

When looking at 1.5Mn and 0.6Mn0.6Cr, the Fe removal potential of 1.5Mn is higher than that of 0.6Mn0.6Cr, while also giving a significantly higher yield. From a process optimisation perspective, 1.5Mn addition represents a more favourable compromise between Fe removal efficiency and yield in low-Fe Al-Si alloys, offering a significantly higher yield at slightly lower Fe removal efficiency than 0.6Mn0.6Cr addition.

3.2.2 Comparison between Mn-Cr and Mn-Sr additions

A comparison between Mn-Cr and Mn-Sr additions was conducted on the micrographs of the sedimented region in the slow-cooled Fe-bearing intermetallic particle analysis sample. It was observed that there were two distinct types of sedimented particles in Mn-Sr additions (Figure 14). The EDS analysis revealed that the dark grey particles are Sr-bearing intermetallic, and the light grey particles are Fe-bearing intermetallic.

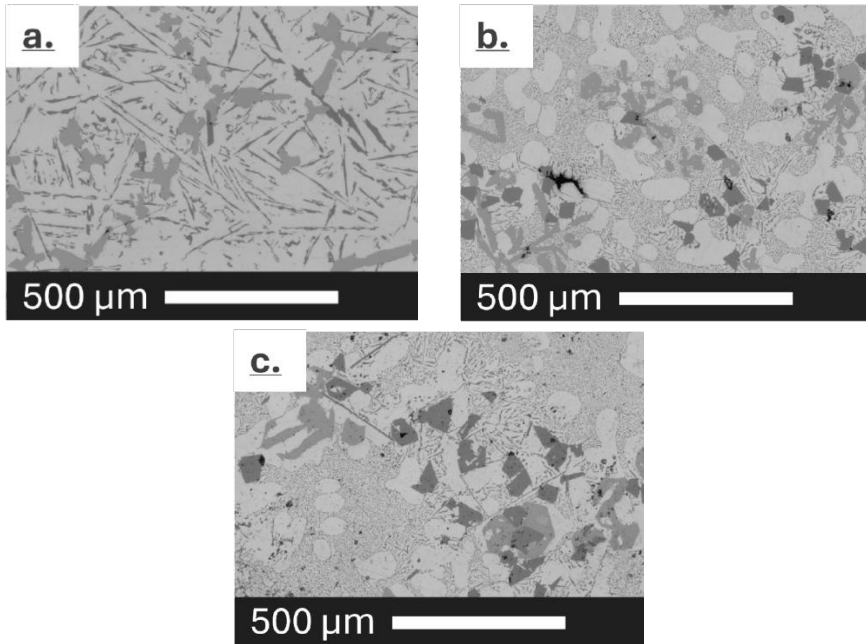


Figure 14. A magnified image of the Fe-bearing intermetallic particle analysis sample's sedimented region (1×2 mm region) for a. $1.2\text{Mn}0.3\text{Cr}$, b. $1.2\text{Mn}0.3\text{Sr}$ and c. $1.2\text{Mn}0.6\text{Sr}$. 'a' shows light grey particles, whereas 'b' and 'c' show two particle populations.

The results for yield, packing density, and elemental composition are summarised in Table 6. Based on the elemental analysis of the intermetallic particles, the Fe content within the Fe-bearing intermetallic particles in all three alloy additions is relatively consistent. While the Mn content in Mn-Sr addition is notably higher. The remaining composition of the Fe-bearing intermetallic particles is aluminium.

Table 6 Summary of particles' yield, packing density and elemental composition of the intermetallic particle sample in 1.2Mn0.3Cr, 1.2Mn0.3Sr and 1.2Mn0.6Sr alloys.

Alloy	Particles	Yield (%)	Packing Density (%)	Intermetallic Particles Composition (wt%)			
				Fe	Mn	Cr	Sr
1.2Mn 0.3Cr	Fe-based	49	8.5 ± 1.3	6.7 ± 0.2	16.4 ± 0.6	5.1 ± 0.4	-
1.2Mn 0.3Sr	Fe-based	92	13.1 ± 1.5	6.9 ± 0.2	21.1 ± 0.2	-	0.9 ± 0.1
	Sr-based	-	-	0.11 ± 0.03	0.10 ± 0.04	-	45.1 ± 0.1
1.2Mn 0.6Sr	Fe-based	86	5.1 ± 1.9	6.9 ± 0.2	20.6 ± 0.3	-	0.9 ± 0.1
	Sr-based	-	-	0.11 ± 0.05	0.11 ± 0.03	-	44.2 ± 0.2

The packing density of the Fe-bearing intermetallic particles (light grey) in the 1.2Mn0.3Sr alloy addition is higher than that of the 1.2Mn0.3Cr addition. This difference results in significantly lower sedimented height in 1.2Mn0.3Sr. This means that Sr addition increases both the particles' packing density and yield, primarily by influencing the morphology and size distribution of the Fe-bearing intermetallic particles [55,70]. When combined with Mn, Sr promotes the formation of a more script-like Fe-bearing intermetallic particle morphology as illustrated in Figure 14b. Whereas Cr addition in combination with Mn changes the morphology of the Fe-bearing intermetallic particles (more dendritic) [70], which increases melt entrapment within the sedimented region and reduces the clean aluminium yield.

Moreover, Sr addition in combination with Mn has been reported to break down larger α -Al₁₅(Fe, Mn)₄Si₂ into smaller fractions, which facilitates tighter particle packing within the sedimented region [55].

However, when Sr is further increased from 0.3 wt% to 0.6 wt%, the clean aluminium yield and the packing density of Fe-bearing intermetallic particles are negatively affected. The decrease in yield and particle packing density is mainly attributed to enhanced formation and sedimentation of the Sr-based intermetallic particles, which do not contribute to the Fe removal efficiency.

In order to better quantify the contribution of the Fe-bearing intermetallic particles and the removal efficiency, the Fe removal potential (ϕ_{Fe}) was calculated using Equation 4, and the results are summarised in Table 7.

Table 7 Fe removal potential calculation for 1.2Mn0.3Cr, 1.2Mn0.3Sr and 1.2Mn0.6Sr alloys.

Alloy	Fe removal potential (%)
1.2Mn0.3Cr	0.31
1.2Mn0.3Sr	0.36
1.2Mn0.6Sr	0.14

The calculated ϕ_{Fe} indicates that the 1.2Mn0.3Sr additions exhibit higher ϕ_{Fe} compared to 1.2Mn0.3Cr additions, primarily due to the considerably higher Fe-bearing intermetallic particles packing density, despite having lower Fe removal efficiency. Moreover, a further increase in Sr from 0.3 to 0.6 wt% negatively affects the ϕ_{Fe} , as the Fe-bearing intermetallic particles' packing density decreases while maintaining nearly similar Fe removal efficiency.

The relationship between ϕ_{Fe} and clean aluminium yield for the three alloy additions demonstrates a clear trade-off between the Fe removal efficiency and yield. The Mn-Cr combination enhances Fe removal efficiency at the expense of the clean aluminium yield. For the Mn-Sr combination, it significantly improves clean aluminium yield but moderately reduces Fe removal efficiency.

From a process optimisation perspective, 1.2Mn0.3Sr addition represents the most favourable compromise, as it provides a significantly higher clean

aluminium yield while only reducing the Fe removal efficiency by around 15% in low-Fe Al-Si alloys.

3.3 Growth and sedimentation behaviour of the Fe-bearing intermetallic particles

The previously performed microstructural analysis (Section 3.2) proves that alloy additions significantly modify the population and morphology of the Fe-bearing intermetallic particles. However, Fe removal depends not only on how many particles form but also on how they grow and sediment at different cooling rates, as well as on the dynamic interaction between growth kinetics and gravitational settling.

To further evaluate the sedimentation behaviour of Fe-bearing intermetallic particles, a physics-based particle growth and sedimentation model was developed. The model was developed to quantitatively describe the coupled evolution of particle size and settling behaviour at different cooling rates.

This was done by integrating the growth kinetics of Fe-bearing intermetallic particles with settling velocity calculations derived from the force balance, since Stokes' law could not be used as the particles are growing. The calibration of this model was performed using experimental measurements of sedimented height, maximum particle height and the area fraction of sedimented Fe-bearing intermetallic particles from the slow-cooling Fe-bearing intermetallic particle analysis sample, since it is near equilibrium.

Based on the force-balance analysis presented in Supplement III, the velocity (v) of the particle that is simultaneously growing and settling can be derived by coupling gravitational driving force with hydrodynamic resistance. Assuming that the particle radius (r) evolves according to a diffusion-controlled growth (Equation 5), the particle's radius is assumed to grow until the Fe-bearing intermetallic particles' equilibrium volume fraction is reached. The time-dependent settling velocity is expressed in Equation 6.

$$r(t) = kt^{1/2} \quad 5$$

$$v(t) = B \frac{t}{A + 1} \quad 6$$

Where k is the growth coefficient, t is time, $A \equiv \frac{3}{2} + \frac{9\eta_v a}{2\rho_p k^2}$, $B \equiv \left(1 - \frac{\rho_\ell}{\rho_p}\right)g$, ρ_p is the density of the Fe-bearing intermetallic particle, ρ_ℓ is the density of the liquid aluminium, a is the correction factor to correct the deviation from spherical shape and other resistive forces acting on the particle (tortuosity, particle interference and particle permeability), η_v is the melt viscosity and g is the gravitational acceleration.

After deriving the settling velocity equation, the growth-sedimentation model was implemented. First, the nucleation sites and the total number of particles (along the x-, y-, and z-axes) were calculated from the experimental analysis of the Fe-bearing intermetallic particle sample for the two different cooling rates, as described in Supplement III. Each particle is assumed to be spherical, starting with a radius equal to zero.

Additionally, a correction factor M was introduced to account for the non-spherical shape and packing effect of a single particle (Equation 7). This correction bridges the idealised spherical growth assumptions with the experimentally observed particle morphological complexity.

$$M = \left(\frac{1}{f_p}\right)^{1/3} \quad 7$$

The parameters k and M were calibrated using the experimental results from the slow-cooled sample, since the Fe-bearing intermetallic particles are near equilibrium. Particles were then allowed to grow while settling at a velocity defined by Equation 6. When the calculated particle volume fraction reaches the equilibrium volume fraction, the particle will stop growing and continue settling at a fixed radius using Stokes' law (Equation 8).

$$v = \frac{2(\rho_P - \rho_L)gr^2}{9\eta_v a} \quad 8$$

Once the particle reaches the settled region, it is assumed to stop growing. The model simulation stops the moment the melt solidifies. The model was not extended to the Mn-Sr addition. This is because the Mn-Sr additions exhibit dual-particle sedimentation behaviour, where Sr-containing intermetallic particles coexist with the Fe-bearing intermetallic particles. Microstructural observations from Supplement II showed that in many cases, the Sr-intermetallic particles are in contact with the Fe-bearing intermetallic particles. This suggests mechanical coupling and cooperative settling mechanisms that are not captured by the current model framework (force balance). Consequently, to model the Mn-Sr addition, a multiparticle interaction approach would be required.

Regarding the fitting parameter a , the slow and fast cooling samples were set to have different a . This is because the Fe-bearing intermetallic particle structure varies with cooling rate, thereby affecting the particles' sedimentation behaviour.

Under slow-cooling conditions, the Fe-bearing intermetallic particles in 0.6Mn0.6Cr and 1.5Mn0.6Cr develop a more pronounced dendritic branching compared to those in the fast-cooling sample (shown in Supplement III). In the 1.5Mn addition case, slow-cooling promotes the formation of a larger plate-like structure of the Fe-bearing intermetallic particles. The changes in the structure of the Fe-bearing intermetallic particles at different cooling rates are supported by Fabrizi et al. [71] and He et al. [72].

The model was calibrated using experimental measurements of the maximum particle height (h_{max}) and the area fraction of the sedimented region of the slow-cooling Fe-bearing intermetallic particle analysis sample, since it is near equilibrium. The correction factors that account for the resistive forces a , sedimented height (h_{sed}) and total particle volume fraction (f) were estimated and the results are shown in Table 8.

Table 8 Model results summary when having different a for different cooling rates for 1.5Mn, 0.6Mn0.6Cr and 1.5Mn0.6Cr.

Alloy	Cooling Rate (°C/min)	a	$h_{sed} (\times 10^{-2} \text{ m})$		$f (\%)$	
			Model	Exp.	Model	Eq.
1.5Mn	30 (slow)	2.8	1.97	1.25	3.00	3.00
	84 (fast)	0.8	0.71	0.69	1.72	3.00
0.6Mn 0.6Cr	30 (slow)	21.4	2.19	1.83	2.50	2.50
	84 (fast)	11.8	0.18	-	1.05	2.50
1.5Mn 0.6Cr	30 (slow)	34.7	1.23	1.34	4.50	4.50
	84 (fast)	12.6	0.17	-	1.56	4.50

In the fast-cooling sample of 1.5Mn, 0.6Mn0.6Cr and 1.5Mn0.6Cr, the f_{model} remained consistently lower than f_{eq} indicating that the equilibrium has not been reached in this cooling condition. While for the slow-cooling condition, f_{model} was equal f_{eq} since the slow-cooling sample was assumed and calibrated to reach equilibrium.

In regard to the h_{sed} , the fast-cooling samples exhibit very small h_{sed} meaning that only a limited fraction of Fe-bearing intermetallic particles reaches the sedimented region before melt solidification. In the fast-cooling samples of 0.6Mn0.6Cr and 1.5Mn0.6Cr, the experimental h_{sed} could not be quantified since a distinct, densely packed sedimented layer did not form before complete solidification. While for the slow-cooling sample, the model slightly overestimates/underestimates the h_{sed} .

When comparing the correction factor that accounts for the resistive force a , the slow-cooling samples exhibit significantly higher values compared to the fast-cooling samples in 1.5Mn, 0.6Mn0.6Cr and 1.5Mn0.6Cr alloy additions. This behaviour supports the findings of Fabrizi et al. [71] and He et al. [72]. In addition to the cooling-rate dependence of a , the resistance parameter varies systematically with alloy chemistry. At the same cooling rate, alloys exhibiting an interconnected or dendritic particle morphology (1.5Mn0.6Cr)

have higher resistive forces than those with sparser, more compact particles (1.5Mn).

To analyse the sedimentation kinetics, the evolution of h_{max} , h_{sed} , and the total particle volume fraction was evaluated over time as shown in Figures 15–17.

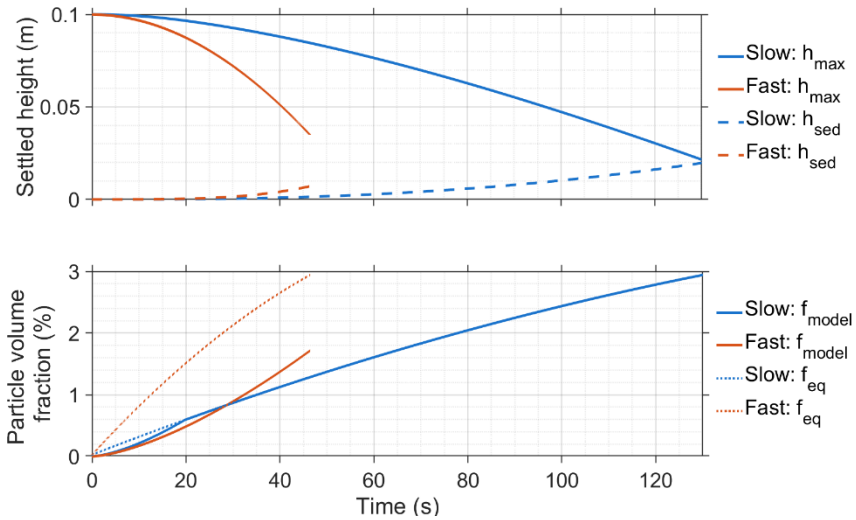


Figure 15. Model-calculated evolution of settled height (top) and particle volume fraction (bottom) for slow and fast cooling, with equilibrium particle volume fraction f_{eq} shown for comparison for 1.5Mn.

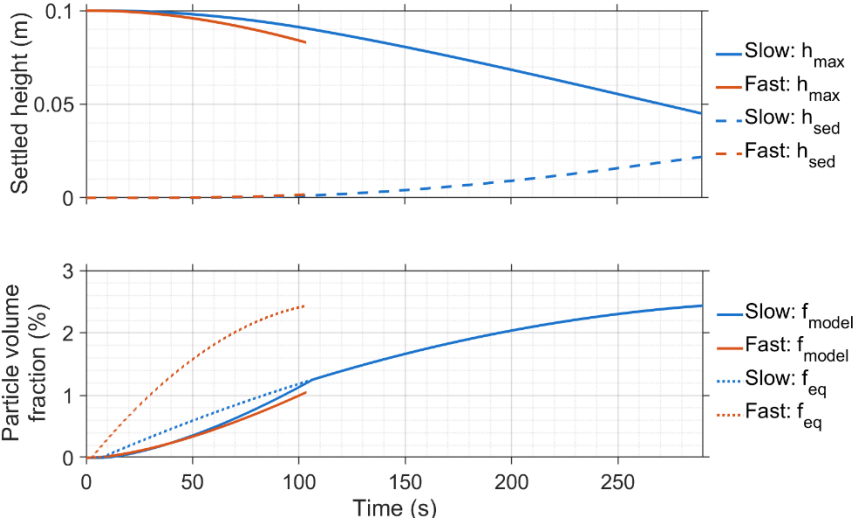


Figure 16. Model-calculated evolution of settled height (top) and particle volume fraction (bottom) for slow and fast cooling, with equilibrium particle volume fraction f_{eq} shown for comparison for 0.6Mn0.6Cr.

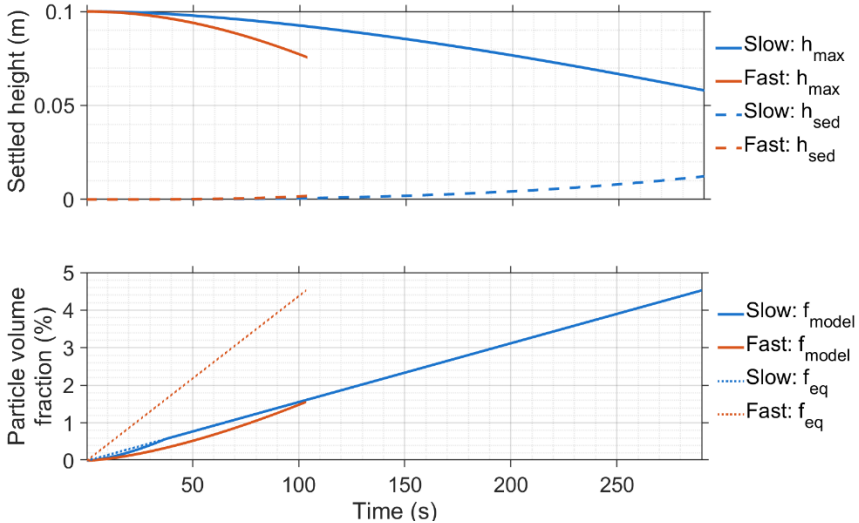


Figure 17. Model-calculated evolution of settled height (top) and particle volume fraction (bottom) for slow and fast cooling, with equilibrium particle volume fraction f_{eq} shown for comparison for 1.5Mn0.6Cr.

The decrease in h_{max} and the increase in h_{sed} in all three cases over time corresponds to progressive particle settling and an increasing clean (particle-free) region. Under fast-cooling conditions, the particle sedimentation progresses more rapidly due to the lower resistance parameter a ; however, the limited growth window restricts total sedimentation. While slow-cooling conditions provide a longer growth and settling window, resulting in a greater final reduction of h_{max} .

Comparisons between f_{model} and f_{eq} in the fast-cooled samples revealed that in all three alloy additions the $f_{model} < f_{eq}$ throughout solidification. This indicates that the particle continues to grow while settling and the equilibrium-constrained regime (Equation 8) is not activated. In contrast, in the slow-cooling sample, f_{model} reaches f_{eq} after approximately 17 s for 1.5Mn (Figure 15), 105 s for 0.6Mn0.6Cr (Figure 16) and 30 s for 1.5Mn0.6Cr (Figure 17).

Once f_{eq} is reached, particle growth becomes equilibrium-limited rather than diffusion-controlled and particle growth occurs every time step rather than continuously. As the temperature decreases f_{eq} increases. The particle grows until reaching the new equilibrium (radius increases) and subsequently settles at a constant radius until the next time step.

These findings are consistent with the observed difference in clean aluminium yield. Although the 1.5Mn0.6Cr alloy addition produced a higher particle population, its lower yield is likely associated with the greater effective resistance to sedimentation, as represented in the model by viscosity effects, tortuosity, particle-particle interactions, and drag. While the 1.5Mn addition has a higher yield, consistent with lower effective resistance and a more compact morphology, allowing for more effective sedimentation.

4 Conclusion

Chapter introduction

This chapter summarises the final conclusions drawn for each research question.

The conclusions are presented for each research question, starting with RQ1 and followed by RQ2 and RQ3.

***RQ1** How does alloy chemistry, particularly Mn, Cr and Sr additions, influence the formation, population and morphology of the Fe-bearing intermetallic particles in low-Fe Al-Si alloys?*

The results in Supplements I and II show that, based on the equilibrium calculations, Mn increases the volume fraction of the Fe-bearing intermetallic particles, and Cr addition increases the formation temperature of the Fe-bearing intermetallic particles.

When looking at the experimental results, 1.5Mn addition increases the particle packing density and generates a more compact polyhedral Fe-bearing intermetallic particle. When combining Mn with Cr, the particle packing density further increases, and the particle morphology changes into a more dendritic morphology in a low-Fe Al-Si alloy. Whereas Sr combined with Mn promotes the formation of a more script-like Fe-bearing intermetallic particle morphology (with the highest particle packing density).

Composition analysis of the Fe-bearing intermetallic particles shows that increasing Mn addition leads to a shift in the intermetallic chemistry towards Mn-rich Fe-bearing intermetallic particles and reduces both Fe and Cr incorporation.

RQ2 *To what extent could the Fe removal in low-Fe Al-Si melt be enhanced through Fe-bearing intermetallic particle former additions and what trade-offs could arise?*

The results in Supplements I and II show that, for a low-Fe Al-Si alloy, the highest Fe removal efficiency is achieved by Mn-Cr additions. Also, increasing Mn at constant Cr increases the onset temperature of Fe reduction and enhances overall Fe removal performance in low-Fe Al-Si alloys.

To establish a relationship between Fe removal efficiency and the Fe-bearing intermetallic particles, the Fe removal potential was calculated. A comparison between the Fe removal potential and clean aluminium yield reveals a clear trade-off: Higher Fe removal efficiency results in lower clean aluminium yield (Mn-Cr addition) and vice versa (Mn-Sr/Mn-only additions).

RQ3 *How do the cooling rate and particle morphology affect growth, interactions and sedimentation behaviour of the Fe-bearing intermetallic particles?*

A physics-based growth-sedimentation model was developed and calibrated using experimental results to quantitatively describe the coupled evolution of particle size and settling behaviour at different cooling rates.

The results show that the cooling rate strongly influences the particle morphology and associated resistive forces acting on the particle during sedimentation. Under slow-cooling conditions, the Fe-bearing intermetallic particles in 0.6Mn0.6Cr and 1.5Mn0.6Cr develop a more pronounced dendritic branching, leading to significantly higher effective resistance compared to fast-cooling conditions. In the 1.5Mn addition case, slow-cooling promotes the formation of a larger and more compact plate-like structure of the Fe-bearing intermetallic particles.

5 Future Work

Chapter introduction

This chapter summarises the limitations and future work of this research.

The research presented in this thesis sheds light on the combined influence of alloy chemistry and cooling conditions on the formation, evolution, and sedimentation of Fe-bearing particles in low-Fe Al-Si alloys. However, to optimise the alloy addition for Fe refining, parameters beyond Fe removal efficiency, clean aluminium yield, and sedimentation rate could be considered. These include the influence of the formed Fe-bearing intermetallic particles on mechanical properties (e.g., RPT and tensile tests), the environmental impact (carbon footprint), and the economic feasibility of the selected alloying strategy compared to conventional recycling routes and primary aluminium production.

With respect to alloy combinations, Mn, Mn-Cr and Mn-Sr combinations were investigated in this thesis. However, the combined effect of Mn-Cr-Sr additions was not explored. Investigating this alloy combination could provide further insight into the potential synergistic interactions between these elements, particularly regarding the morphology and distribution of Fe-bearing intermetallic particles and Fe removal efficiency.

Furthermore, the developed growth-sedimentation model was primarily used as a descriptive model calibrated with experimental analysis. To evaluate the model's true predictive capability, additional controlled experiments across varied cooling rates and alloy compositions could be conducted for independent validation. Additionally, this growth-sedimentation model assumes simplified particle geometry and effective resistance parameters; further developments should incorporate 3D particle morphology and explicit particle-to-particle interaction (Mn-Sr addition case). Moreover, further

model development could incorporate the influence of melt convection and turbulence-driven particle settling, as industrial-scale melts are rarely static.

Finally, the sedimented intermetallic-rich region represents a material stream with high intermetallic concentrations and potential functional value. Further research could explore ways to dispose of or reuse the residuals for either additive manufacturing purposes or composite reinforcement.

References

- [1] J. Wu, F. Djavanroodi, C. Gode, S. Attarilar, M. Ebrahimi, Melt refining and purification processes in Al alloys: a comprehensive study, *Mater. Res. Express* 9 (2022) 032001. <https://doi.org/10.1088/2053-1591/ac5b03>.
- [2] T. Hiraki, T. Miki, K. Nakajima, K. Matsubae, S. Nakamura, T. Nagasaka, Thermodynamic Analysis for the Refining Ability of Salt Flux for Aluminum Recycling, *Materials* 7 (2014) 5543–5553. <https://doi.org/10.3390/ma7085543>.
- [3] D. Raabe, D. Ponge, P.J. Uggowitzer, M. Roscher, M. Paolantonio, C. Liu, H. Antrekowitsch, E. Kozeschnik, D. Seidmann, B. Gault, F. De Geuser, A. Deschamps, C. Hutchinson, C. Liu, Z. Li, P. Prangnell, J. Robson, P. Shanthraj, S. Vakili, C. Sinclair, L. Bourgeois, S. Pogatscher, Making sustainable aluminum by recycling scrap: The science of “dirty” alloys, *Prog. Mater. Sci.* 128 (2022) 100947. <https://doi.org/10.1016/j.pmatsci.2022.100947>.
- [4] J.M. Cullen, J.M. Allwood, Mapping the Global Flow of Aluminum: From Liquid Aluminum to End-Use Goods, *Environ. Sci. Technol.* 47 (2013) 3057–3064. <https://doi.org/10.1021/es304256s>.
- [5] S.K. Das, J.G. Kaufman, Aluminum Recycling: Economic and Environmental Benefits, *Light Metal Age* 68 (2010). <https://api.semanticscholar.org/CorpusID:19776134>.
- [6] G. Gaustad, E. Olivetti, R. Kirchain, Improving aluminum recycling: A survey of sorting and impurity removal technologies, *Resour. Conserv. Recycl.* 58 (2012) 79–87. <https://doi.org/10.1016/j.resconrec.2011.10.010>.
- [7] S. Schlacke, H. Wentzien, E.-M. Thierjung, M. Köster, Implementing the EU Climate Law via the ‘Fit for 55’ package, *Oxford Open Energy* 1 (2022). <https://doi.org/10.1093/ooenergy/oiab002>.

- [8] Yu.N. Mansurov, N. V. Letyagin, A.S. Finogeyev, J.U. Rakhmonov, Influence of impurity elements on the casting properties of Al – Mg based alloys, *Non-Ferrous Metals* (2018) 24–29. <https://doi.org/10.17580/nfm.2018.01.05>.
- [9] M. Durmuş, D. Dispınar, M. Gavgali, E. Uslu, M. Çolak, Evaluation of Fe Content on the Fluidity of A356 Aluminum Alloy by New Fluidity Index, *International Journal of Metalcasting* 19 (2025) 1590–1604. <https://doi.org/10.1007/s40962-024-01396-4>.
- [10] O. Majidi, S.G. Shabestari, M.R. Aboutalebi, Study of fluxing temperature in molten aluminum refining process, *J. Mater. Process. Technol.* 182 (2007) 450–455. <https://doi.org/10.1016/j.jmatprotec.2006.09.003>.
- [11] S. Otarawanna, A.K. Dahle, Casting of aluminium alloys, in: *Fundamentals of Aluminium Metallurgy*, Elsevier, 2011: pp. 141–154. <https://doi.org/10.1533/9780857090256.1.141>.
- [12] J. Park, M.G. Kim, J.H. Kim, J. Shin, K.L. wLee, Continuous Casting of Hypereutectic Aluminum-Silicon Alloy Billets Using Electromagnetic Stirring Technique, *IOP Conf. Ser. Mater. Sci. Eng.* 424 (2018) 012054. <https://doi.org/10.1088/1757-899X/424/1/012054>.
- [13] B.G. Dietrich, H. Becker, M. Smolka, A. Keßler, A. Leineweber, G. Wolf, Intermetallic Sludge Formation in Fe Containing Secondary Al-Si Alloys Influenced by Cr and Mn as Preparative Tool for Metal Melt Filtration, *Adv. Eng. Mater.* 19 (2017) 1700161. <https://doi.org/10.1002/adem.201700161>.
- [14] R. Podprocká, D. Bolibruchová, M. Chalupová, Reducing the Negative of the Iron in the Alloy Based on Al-Si-Mg by Manganese, *Archives of Foundry Engineering* 17 (2017) 212–216. <https://doi.org/10.1515/afe-2017-0077>.
- [15] L. Zhang, J. Gao, L.N.W. Damoah, D.G. Robertson, Removal of Iron From Aluminum: A Review, *Mineral Processing and Extractive*

Metallurgy Review 33 (2012) 99–157.
<https://doi.org/10.1080/08827508.2010.542211>.

- [16] G.S. Gontijo, A.C.B. de Araújo, S. Prasad, L.G.S. Vasconcelos, J.J.N. Alves, R.P. Brito, Improving the Bayer Process productivity – An industrial case study, *Miner. Eng.* 22 (2009) 1130–1136. <https://doi.org/10.1016/j.mineng.2009.04.010>.
- [17] A.M. Donoghue, N. Frisch, D. Olney, Bauxite Mining and Alumina Refining, *J. Occup. Environ. Med.* 56 (2014) S12–S17. <https://doi.org/10.1097/JOM.0000000000000001>.
- [18] A.P. Ratvik, R. Mollaabbasi, H. Alamdari, Aluminium production process: from Hall–Héroult to modern smelters, *ChemTexts* 8 (2022) 10. <https://doi.org/10.1007/s40828-022-00162-5>.
- [19] H. Demirpolat, R. Binali, M. Kuntoğlu, E. Salur, M.A. Makhesana, S. Yaghoubi, Ü.A. Usca, The influences of alloying elements and processing conditions on the machinability of wrought aluminium alloys: A literature review, *Proceedings of the Institution of Mechanical Engineers, Part E: Journal of Process Mechanical Engineering* (2024). <https://doi.org/10.1177/09544089241290395>.
- [20] M. Di Sabatino, L. Arnberg, Castability of aluminium alloys, *Transactions of the Indian Institute of Metals* 62 (2009) 321–325. <https://doi.org/10.1007/s12666-009-0049-2>.
- [21] S. Majumdar, A. Sinha, A. Das, P. Datta, D. Nag, An Insight View of Evolution of Advanced Aluminum Alloy for Aerospace and Automotive Industry: Current Status and Future Prospects, *Journal of The Institution of Engineers (India): Series D* (2024). <https://doi.org/10.1007/s40033-024-00852-z>.
- [22] J. Olofsson, I.L. Svensson, Incorporating predicted local mechanical behaviour of cast components into finite element simulations, *Mater. Des.* 34 (2012) 494–500. <https://doi.org/10.1016/j.matdes.2011.08.029>.

- [23] D.K. Dwivedi, R. Sharma, A. Kumar, Influence of silicon content and heat treatment parameters on mechanical properties of cast Al–Si–Mg alloys, *International Journal of Cast Metals Research* 19 (2006) 275–282. <https://doi.org/10.1179/136404606X153867>.
- [24] P. Biswas, S. Patra, M. Mondal, Structure-property correlation of eutectic Al-12.4 Si alloys with and without Zirconium (Zr) addition, *International Journal of Cast Metals Research* 33 (2020) 1–12. <https://doi.org/10.1080/13640461.2020.1769319>.
- [25] J. CUI, H.J. ROVEN, Recycling of automotive aluminum, *Transactions of Nonferrous Metals Society of China* 20 (2010) 2057–2063. [https://doi.org/10.1016/S1003-6326\(09\)60417-9](https://doi.org/10.1016/S1003-6326(09)60417-9).
- [26] S. Roy, L.F. Allard, A. Rodriguez, W.D. Porter, A. Shyam, Comparative Evaluation of Cast Aluminum Alloys for Automotive Cylinder Heads: Part II—Mechanical and Thermal Properties, *Metallurgical and Materials Transactions A* 48 (2017) 2543–2562. <https://doi.org/10.1007/s11661-017-3986-0>.
- [27] J.M. Sanchez, M. Arribas, H. Galarraga, M. Garcia de Cortazar, M. Ellero, F. Girot, Effects of Mn addition, cooling rate and holding temperature on the modification and purification of iron-rich compounds in AlSi10MnMg(Fe) alloy, *Heliyon* 9 (2023) e13005. <https://doi.org/10.1016/j.heliyon.2023.e13005>.
- [28] T. Keijer, V. Bakker, J.C. Slootweg, Circular chemistry to enable a circular economy, *Nat. Chem.* 11 (2019) 190–195. <https://doi.org/10.1038/s41557-019-0226-9>.
- [29] S.H. Farjana, N. Huda, M.A.P. Mahmud, Impacts of aluminum production: A cradle to gate investigation using life-cycle assessment, *Science of The Total Environment* 663 (2019) 958–970. <https://doi.org/10.1016/j.scitotenv.2019.01.400>.
- [30] L. Zhang, X. Lv, A.T. Torgerson, M. Long, Removal of Impurity Elements from Molten Aluminum: A Review, *Mineral Processing and Extractive Metallurgy Review* 32 (2011) 150–228. <https://doi.org/10.1080/08827508.2010.483396>.

- [31] B. Wan, W. Li, F. Liu, T. Lu, S. Jin, K. Wang, A. Yi, J. Tian, W. Chen, Determination of fluoride component in the multifunctional refining flux used for recycling aluminum scrap, *Journal of Materials Research and Technology* 9 (2020) 3447–3459. <https://doi.org/10.1016/j.jmrt.2020.01.082>.
- [32] T. Kékesi, International Motivation and Cooperation for Research in the Ultra-High Purification of Metals, *Eur. Integr. Stud* (2002) 109–126.
- [33] M. Gotenbruck, D.C. Curtolo, S. Friedrich, B. Friedrich, The Effectiveness of Cooled-Finger and Vacuum Distillation Processes in View of the Removal of Fe, Si and Zn from Aluminium, *Metals (Basel)*. 12 (2022) 2027. <https://doi.org/10.3390/met12122027>.
- [34] M. Dada, P. Popoola, Recent advances in joining technologies of aluminum alloys: a review, *Discov. Mater.* 4 (2024) 86. <https://doi.org/10.1007/s43939-024-00155-w>.
- [35] C.B. Basak, N. Hari Babu, Morphological changes and segregation of β -Al 9 Fe 2 Si 2 phase: A perspective from better recyclability of cast Al-Si alloys, *Mater. Des.* 108 (2016) 277–288. <https://doi.org/10.1016/j.matdes.2016.06.096>.
- [36] H.R. Kotadia, N. Bareker, M.H. Khan, J.I. Ahuir-Torres, A. Das, Aluminium recycling: A critical review of iron-bearing intermetallics in aluminium alloys, *Materials Today Sustainability* 30 (2025) 101119. <https://doi.org/10.1016/j.mtsust.2025.101119>.
- [37] M.M. Vicent Fanconi, I. Gil Fernández-Marcote, Í. Ruiz-Bustanza, The Challenge of Impurities (Fe, Si) to Recycling in the Rolled Aluminum Industry in the Coming Years in Relation to Their Influence on Ultimate Tensile Strength, *Metals (Basel)*. 13 (2023) 2014. <https://doi.org/10.3390/met13122014>.
- [38] C.M. Dinnis, J.A. Taylor, A.K. Dahle, As-cast morphology of iron-intermetallics in Al–Si foundry alloys, *Scr. Mater.* 53 (2005) 955–958. <https://doi.org/10.1016/j.scriptamat.2005.06.028>.

- [39] K.C. Williams, M.J. Mallaburn, M. Gagola, M.D. O’Toole, R. Jones, A.J. Peyton, Classification of Shredded Aluminium Scrap Metal Using Magnetic Induction Spectroscopy, *Sensors* 23 (2023) 7837. <https://doi.org/10.3390/s23187837>.
- [40] D. Díaz-Romero, S. Van den Eynde, I. Zaplana, C. Zhou, W. Sterkens, T. Goedemé, J. Peeters, Classification of aluminum scrap by laser induced breakdown spectroscopy (LIBS) and RGB + D image fusion using deep learning approaches, *Resour. Conserv. Recycl.* 190 (2023) 106865. <https://doi.org/10.1016/j.resconrec.2023.106865>.
- [41] Y. Wu, T. Oudshoorn, P. Rem, Modelling and optimization of an innovative facility for automated sorting of aluminium scraps, *Waste Management* 189 (2024) 103–113. <https://doi.org/10.1016/j.wasman.2024.08.018>.
- [42] A.K. Prasada Rao, W.Q. Ain, M.K. Faisal, B.I. Mazni, Undiluted Recycling of Aluminum Scrap Alloy Using Hume-Rothery’s Rule, *Metallography, Microstructure, and Analysis* 7 (2018) 239–244. <https://doi.org/10.1007/s13632-018-0431-8>.
- [43] D. Paraskevas, G. Ingarao, Y. Deng, J.R. Duflou, Y. Pontikes, B. Blanpain, Evaluating the material resource efficiency of secondary aluminium production: A Monte Carlo-based decision-support tool, *J. Clean. Prod.* 215 (2019) 488–496. <https://doi.org/10.1016/j.jclepro.2019.01.097>.
- [44] D. Paraskevas, K. Kellens, W. Dewulf, J. Duflou, Closed and Open Loop Recycling of Aluminium: A Life Cycle Assessment perspective, in: 2013.
- [45] R. Kieft, T. Bergstrom, P. Le Brun, B. Friedrich, A. Oygard, A. Pisch, G. Rombach, M. Ryckeboer, W. De Schutter, Aluminium purification, in: *ASEM Workshop on Clean Technologies, Hanoi, 2004*: pp. 1–10.
- [46] G. Liu, Y. Ren, W. Ma, K. Morita, Y. Lei, S. Zhan, G. Lv, S. Li, Z. Wang, R. Li, Recent advances and future trend of aluminum alloy melt purification: A review, *Journal of Materials Research and Technology* 28 (2024) 4647–4662. <https://doi.org/10.1016/j.jmrt.2024.01.024>.

- [47] M.A. Dewan, M.A. Rhamdhani, J.B. Mitchell, C.J. Davidson, G.A. Brooks, M. Easton, J.F. Grandfield, Control and Removal of Impurities from Al Melts: A Review, *Materials Science Forum* 693 (2011) 149–160.
<https://doi.org/10.4028/www.scientific.net/MSF.693.149>.
- [48] S. Capuzzi, G. Timelli, L. Capra, L. Romano, Study of fluxing in Al refining process by rotary and crucible furnaces, *International Journal of Sustainable Engineering* 12 (2019) 38–46.
<https://doi.org/10.1080/19397038.2017.1393022>.
- [49] J.A. Taylor, Iron-Containing Intermetallic Phases in Al-Si Based Casting Alloys, *Procedia Materials Science* 1 (2012) 19–33.
<https://doi.org/10.1016/j.mspro.2012.06.004>.
- [50] B. Zeng, C. Chen, H. Zhao, C. Zhang, P. Liu, G. Wang, A. He, F. Liu, A systematic review of the production of high-purity aluminum: Applications, preparation, and mechanisms, *Journal of Materials Research and Technology* 34 (2025) 987–1009.
<https://doi.org/10.1016/j.jmrt.2024.12.085>.
- [51] D.C. Curtolo, N. Xiong, S. Friedrich, B. Friedrich, High- and Ultra-High-Purity Aluminum, a Review on Technical Production Methodologies, *Metals (Basel)*. 11 (2021) 1407.
<https://doi.org/10.3390/met11091407>.
- [52] K. Luo, Z. Wang, L. Meng, Z. Guo, Removal of iron for aluminum recovery from scrap aluminum alloy by supergravity separation with manganese addition, *Chemical Engineering and Processing - Process Intensification* 173 (2022) 108841.
<https://doi.org/10.1016/j.cep.2022.108841>.
- [53] X. Zhang, D. Wang, H. Nagaumi, R. Wang, Z. Wu, X. Li, H. Zhang, Highly efficient Fe separation induced by Fe-containing particle agglomeration in Al-7Si-0.3Mg alloy melt, *Journal of Materials Research and Technology* 21 (2022) 604–616.
<https://doi.org/10.1016/j.jmrt.2022.09.034>.

- [54] D. Song, Y. Zhao, Z. Wang, Y. Jia, H. Huang, D. Zhang, W. Zhang, Effect of Mn/Fe ratio on Fe removal efficiency and tensile ductility of an Al–7.0Si–2.4Fe alloy, *J. Mater. Res.* 36 (2021). <https://doi.org/10.1557/s43578-021-00194-6>.
- [55] J. Mathew, P. Srirangam, The Effect of Manganese and Strontium on Iron Intermetallics in Recycled Al-7% Si Alloy, in: 2019: pp. 235–240. https://doi.org/10.1007/978-3-030-05864-7_31.
- [56] S. Ferraro, A. Fabrizi, G. Timelli, Evolution of sludge particles in secondary die-cast aluminum alloys as function of Fe, Mn and Cr contents, *Mater. Chem. Phys.* 153 (2015) 168–179. <https://doi.org/10.1016/j.matchemphys.2014.12.050>.
- [57] M.K. Sinha, B. Mishra, S.K. Das, T. Grosko, Influence of Si, Mn, and Cr on the Iron Removal from Aluminum Scrap: A Thermodynamic and Experimental Analysis, *JOM* 77 (2025) 8331–8344. <https://doi.org/10.1007/s11837-025-07640-4>.
- [58] W. YANG, F. GAO, S. JI, Formation and sedimentation of Fe-rich intermetallics in Al–Si–Cu–Fe alloy, *Transactions of Nonferrous Metals Society of China* 25 (2015) 1704–1714. [https://doi.org/10.1016/S1003-6326\(15\)63776-1](https://doi.org/10.1016/S1003-6326(15)63776-1).
- [59] Š. Michna, A. Knaislová, J. Svobodová, J. Novotný, L. Michnová, Possibility of Eliminating Iron in Aluminium Alloy Through Sedimentation, *Manufacturing Technology* 24 (2024) 802–810. <https://doi.org/10.21062/mft.2024.082>.
- [60] J.P. Schoß, H. Becker, A. Keßler, A. Leineweber, G. Wolf, Removal of Iron from a Secondary Al–Si Die-Casting Alloy by Metal Melt Filtration in a Laboratory Filtration Apparatus, *Adv. Eng. Mater.* 24 (2022) 2100695. <https://doi.org/10.1002/adem.202100695>.
- [61] Y. Zhang, Y. Lei, Y. Ren, W. Ma, Removal of Fe impurities from Al alloy scraps by electromagnetic directional solidification combined with Si addition, *Journal of Materials Research and Technology* 26 (2023) 8738–8747. <https://doi.org/10.1016/j.jmrt.2023.09.163>.

- [62] Y. Sun, X. Huang, C. Liu, M. Zhou, X. Zhang, Impurity iron separation from molten secondary aluminum by pulsed electric current, *J. Alloys Compd.* 934 (2023) 167903. <https://doi.org/10.1016/j.jallcom.2022.167903>.
- [63] L. Zhang, S. Wang, A. Dong, J. Gao, L.N.W. Damoah, Application of Electromagnetic (EM) Separation Technology to Metal Refining Processes: A Review, *Metallurgical and Materials Transactions B* 45 (2014) 2153–2185. <https://doi.org/10.1007/s11663-014-0123-y>.
- [64] Thermo-Calc Software TCAL8/Al-alloys Database version 8.2, (n.d.). <https://thermocalc.com/products/databases/aluminum-based-alloys/> (accessed June 27, 2024).
- [65] P. Johannesson, E. Perjons, *An Introduction to Design Science*, Springer International Publishing, Cham, 2014. <https://doi.org/10.1007/978-3-319-10632-8>.
- [66] Kirsty Williamson, Amanda Bow, *Research methods for students, academics and professionals: information management and systems*, Centre for Information Studies, Charles Sturt University, 2002.
- [67] N.M. Anas, S.A. Zakaria, A.S. Anasyida, H. Mohamad, B.K. Dhindaw, Influence of Semisolid and Strontium Addition on Dry Sliding Wear Behavior of Hypoeutectic Al-Si Alloy, *Archives of Metallurgy and Materials* (2022) 307–317. <https://doi.org/10.24425/amm.2023.141507>.
- [68] H.R. Lashgari, M. Emany, A. Razaghian, A.A. Najimi, The effect of strontium on the microstructure, porosity and tensile properties of A356–10%B4C cast composite, *Materials Science and Engineering: A* 517 (2009) 170–179. <https://doi.org/10.1016/j.msea.2009.03.072>.
- [69] Z. Que, C. Fang, Z. Fan, Nucleation competition and phase transformation mechanisms in recycled aluminium alloys: Insights into θ -Al₁₃Fe₄, Al₆(Fe,Mn) and α -Al₁₅(Fe,Mn)₃Si₂, *J. Alloys Compd.* 1032 (2025) 181130. <https://doi.org/10.1016/j.jallcom.2025.181130>.

- [70] M. Wang, W. Xu, Q. Han, Study of Refinement and Morphology Change of AlFeSi Phase in A380 Alloy due to Addition of Ca, Sr/ Ca, Mn and Mn, Sr, Mater. Trans. 57 (2016) 1509–1513. <https://doi.org/10.2320/matertrans.M2015329>.
- [71] A. Fabrizi, G. Timelli, S. Ferraro, F. Bonollo, Evolution of Fe-rich compounds in a secondary Al–Si–Cu alloy: influence of cooling rate, International Journal of Materials Research 106 (2015) 719–724. <https://doi.org/10.3139/146.111238>.
- [72] W. He, Y. Zhao, Q. Wei, H. Liu, D. Song, Z. Sun, Effect of cooling rates and Fe contents on microstructure evolution of Al-Cu-Mn-Mg-Fe-Si alloys, Mater. Charact. 214 (2024) 114074. <https://doi.org/10.1016/j.matchar.2024.114074>.

Iron Refining in Recycled Al-Si Alloys by Intermetallic Precipitation

Future Al supply is expected to rely increasingly on recycled Al, driven by its lower energy demand and the need to reduce carbon emissions due to stricter environmental regulations and policies. One of the main barriers, however, is the presence of iron (Fe) impurities in recycled Al-Si alloys. Fe promotes the formation of a brittle Fe-bearing intermetallic phase that severely degrades both casting and the mechanical properties of the cast Al. This makes impurity control essential for wider use of recycled aluminium.

This thesis explores how Fe can be refined in low-Fe Al-Si alloys through the addition of manganese (Mn), chromium (Cr) and strontium (Sr), by combining carefully designed experiments with quantitative analysis of the formation and sedimentation behaviour of Fe-bearing intermetallic particles under different Mn, Cr, and Sr combinations.

The results demonstrated that, for a low-Fe Al-Si alloy, a relationship between Fe removal efficiency and the Fe-bearing intermetallic particles was established by calculating the Fe removal potential. Comparison between the Fe removal potential and clean aluminium yield reveals a clear trade-off: higher Fe removal efficiency results in lower clean aluminium yield (Mn-Cr addition) and vice versa (Mn-Sr/Mn-only additions).

To further understand the effect of cooling rate on the Fe-bearing intermetallic, a physics-based growth-sedimentation model was developed and calibrated using experimental results to describe the coupled evolution of particle size quantitatively and settling behaviour at different cooling rates.

By linking alloy chemistry, particle behaviour, Fe removal and yield, this work provides insight into Fe refining in recycled low-Fe Al-Si alloys.



ABDULLAH HARAZEEN is currently a PhD student in the Department of Materials and Manufacturing at the School of Engineering, Jönköping University. He holds a master's degree in Engineering Materials Science from KTH Royal Institute of Technology, with a focus on Sustainability. His research interests lie in the field of material science and processing.

ISBN 978-91-89785-35-9 (Printed version)

ISBN 978-91-89785-36-6 (Online version)